Ocean Modelling 103 (2016) 98–117

Contents lists available at ScienceDirect

Ocean Modelling

journal homepage: www.elsevier.com/locate/ocemod

Virtual Special Issue
Ocean Surface Waves

Wave spectral response to sudden changes in wind direction in finite-depth waters

Saima Aijaz [a,*], W. Erick Rogers [b], Alexander V. Babanin [a]

[a] Centre for Ocean Engineering, Science and Technology, Swinburne University of Technology, Melbourne, Australia
[b] Oceanography Division, Naval Research Laboratory, Stennis Space Center, MS, USA

ARTICLE INFO

Article history:
Received 5 February 2015
Revised 22 October 2015
Accepted 2 November 2015
Available online 14 November 2015

Keywords:
Wave modelling
Wind shift
Wave response
Whitecapping dissipation
Swell dissipation
Bottom friction

ABSTRACT

The response of a wind-sea spectrum to sudden changes in wind directions of 180° and 90° is investigated. Numerical simulations using the third-generation wave spectral model SWAN have been undertaken at micro timescales of 30 s and fine spatial resolution of less than 10 m. The results have been validated against the wave data collected during the field campaign at Lake George, Australia. The newly implemented 'ST6' physics in the SWAN model has been evaluated using a selection of bottom-friction terms and the two available functions for the nonlinear energy transfer: (1) exact solution of the nonlinear term (XNL), and (2) discrete interactions approximation (DIA) that parameterizes the nonlinear term. Good agreement of the modelled data is demonstrated directly with the field data and through the known experimental growth curves obtained from the extensive Lake George data set.

The modelling results show that of the various combinations of models tested, the ST6/XNL model provides the most reliable computations of integral and spectral wave parameters. When the winds and waves are opposing (180° wind turn), the XNL is nearly twice as fast in the aligning the young wind-sea with the new wind direction than the DIA. In this case, the young wind-sea gradually decouples from the old waves and forms a new secondary peak. Unlike the 180° wind turn, there is no decoupling in the 90° wind turn and the entire spectrum rotates smoothly in the new direction. In both cases, the young wind-sea starts developing in the new wind direction within 10 min of the wind turn for the ST6 while the directional response of the default physics lags behind with a response time that is nearly double of ST6.

The modelling results highlight the differences in source term balance among the different models in SWAN. During high wind speeds, the default settings provide a larger contribution from the bottom-friction dissipation than the whitecapping. In contrast, the whitecapping dissipation is dominant in ST6 while the bottom-friction generated by the new model with ripple formation provides a significant contribution during strong winds only. During low wind speeds and non-breaking wave conditions, a separate swell or non-breaking dissipation source term continues the decay of waves that cannot be dissipated by the whitecapping dissipation function.

© 2015 Elsevier Ltd. All rights reserved.

1. Introduction

Wave growth in response to varying wind fields was studied during the JONSWAP field experiment (Hasselmann et al., 1973) in the North Sea, and the more recent field experiments, conducted at Lake George, Australia (Young and Verhagen, 1996; Young, 1999). For the first time under field conditions, the Lake George project obtained estimates of the spectral distribution of the wave breaking dissipation (Babanin and Young, 2005; Manasseh et al., 2006; Young and Babanin, 2006a). Measurements of the wind-input spectral function were conducted at moderate-to-strong wind forcing (Young et al., 2005), and the outcomes were parameterized as source functions suitable for spectral wave models (Donelan et al., 2005, 2006; Babanin et al., 2007). The input and dissipation source functions exhibited a number of physical features that were not previously accounted for. These have been implemented in the third-generation models (Babanin et al., 2010; Tsagareli et al., 2010; Rogers et al., 2012; Zieger et al., 2015) and have resulted in considerable improvement

* Corresponding author at: Swinburne University of Technology, John Street, Hawthorn, VIC 3122, Australia. Tel.: +61 3 9214 4904.
E-mail address: saijaz@swin.edu.au, saimaa2k@yahoo.com (S. Aijaz).

http://dx.doi.org/10.1016/j.ocemod.2015.11.006
1463-5003/© 2015 Elsevier Ltd. All rights reserved.

in the prediction of the wave energy and spectral downshifting of energy in the wave models (Zieger et al., 2015).

However, modelling of the directional response of waves due to sudden changes in wind direction, particularly in shallow coastal waters still remains a challenge. This is mainly because of the complex physics of the shallow water environment and the paucity of wind and wave measurements at finer time scales of few minutes within which the sudden wind changes occur. Such measurements are essential for the testing, calibration, and validation of wave models. In particular, when existing parameterizations are generally based on data where sudden wind shifts may not have been accounted for. Further, the dynamics of shallow water are more complicated than deep water considering the interactions with the coast and the sea-bed, the influence of local wind, and the enhancement of whitecapping and nonlinear interactions (Young, 1988).

In spectral wave models, the growth in wave energy is governed by the energy transfer equation where physical processes are described by individual source terms. The sum of all source terms determines the spectral evolution. Although all source terms contribute to the balance of the source terms, Young and van Vledder (1993) have demonstrated that the nonlinear term plays a central role in development of the spectrum and acts to balance the other source terms. The influence of the nonlinear term is especially dominant for sudden and large wind shifts (Young et al., 1987; van Vledder and Holthuijsen, 1993) where the nonlinear interactions enable the transfer of energy from the old wave system into the new developing young wind-sea.

The response of the wave spectrum for a sequence of wind-direction changes ranging from 30° to 180° has been investigated by Young et al. (1987) using numerical simulations. The simulations consisted of academic exercises with a third-generation model, 3G-WAM using discrete interaction parameterization and the Exact-NL (Hasselmann and Hasselmann, 1982) model with exact solutions for the nonlinear term. Their experiments were simplified by using a constant wind speed as the driving wind field in one-dimensional mode. In the absence of relevant field data, only a qualitative agreement was shown with the analyses of JONSWAP field measurements. The results indicated that for wind shifts of less than 90°, the high frequency components rapidly rotate to align with the new wind direction. For wind shifts of greater than 90°, there is no tendency for the spectrum to rotate in the new direction. Instead, a new secondary peak develops in the young wind-sea resulting in a bimodal spectrum. However, analysis of measured directional spectra during hurricanes from buoys in Western Australia did not indicate any bimodal peaks in either frequency or direction (Young, 2006).

While most of the earlier studies recognize the importance of the nonlinear interactions during wind shifts, there have been limited numerical studies using exact solutions of the nonlinear term in two-dimensional models, in particular for finite-depth waters. In addition to the complexities of shallow water dynamics, the intensive computational effort required for exact computations has been a major issue. With the recent technological advances in the development of parallel processing protocols and high performance computing that enable computations to be distributed among multiple cores and multiple processors of a computer, the application of two-dimensional models with exact solutions has now become more practical, albeit with limited domains or limited resolutions.

Previous studies (Hasselmann et al., 1980; van Vledder and Holthuijsen, 1993; Quanduo and Komen, 1993) of wave response to turning winds have generally been conducted in deep waters. A correction method was developed by van Vledder and Holthuijsen (1993) to handle inhomogeneities in the wave field, which have multiple causes, e.g. swells, radiative effects, wind inhomogeneities. Other constraints applied to the above models included the omission of events where the differences in mean wave direction and the local wind were more than 90°. This was done to reduce noise in the modelled waves resulting from slanting fetch conditions.

Most of the earlier studies mentioned above have been validated against observations of buoy data or remote sensing data, which are usually averaged at intervals of 20 min to few hours. Such observations are unable to account for the wind turns that may occur within a span of few minutes or seconds.

The present study differs fundamentally from the approach of previous studies (e.g. van Vledder and Holthuijsen, 1993) in that the modelling generates a two-dimensional non-homogeneous wave field albeit with spatially uniform wind conditions that vary in time.

This study seeks to investigate the wave response in finite-depth waters due to sudden changes in wind by conducting numerical simulations at high temporal and spatial resolutions using a third-generation spectral model. The nonlinear interactions are studied by the application of both the exact solution (XNL) and the discrete approximate interactions (DIA) methods using high performance parallel computing. The use of the wind and wave data for this study from the Lake George experimental site overcomes many of the issues associated with swell, slanting fetch, and wind variability over fetch encountered in open ocean and coastal areas. Lake George is an endorheic lake or a closed basin where there is no outflow (or inflow) to the rivers or the ocean. The study site at Lake George is thus free from swell contamination. An almost flat bathymetry and a fairly uniform wind across the large fetches of 10–20 km provide nearly ideal conditions for fetch-limited and depth-limited wind-generated wave measurements at Lake George. Nevertheless interactions with the bottom are an issue and have been examined in this study by including a new bottom-friction model (Smith et al., 2011) that explicitly accounts for site-specific physical parameters including grain size, specific gravity of the bed material, ripple formation, and sheet flow.

The purpose of the study is to employ modelling techniques that will lead to improvements in the predictive modelling of rapid wind shifts when the angles between the wind and the waves are large in finite-depth waters. This has strong implications for tropical cyclones where sudden wind shifts are ubiquitous. Rapid changes in wind direction occur frequently in milder conditions also, as will be described in this study.

This study analyses the wave response to sudden wind turning when the difference between the new wind direction and the existing wave direction is 90° and greater. Numerical experiments using the third-generation model, Simulating WAves Nearshore (SWAN) (Booij et al., 1999; SWAN Team, 2014), have been undertaken for two specific wind-shift events: (1) wind turning by 180°; and (2) wind turning by 90°. The objectives of the study are to evaluate the effectiveness of the new physics implemented in the third-generation models for the purpose of predicting the spectral response of the waves to turning winds at microscales of time and space; and to validate the model results with direct field observations at Lake George, Australia. Whilst the new physics (referred to as 'ST6') has been implemented both in SWAN (Rogers et al., 2012) and WAVEWATCH III® (Tolman, 2014; Zieger et al., 2015), SWAN has been selected for this study because the implicit numerical schemes employed in SWAN have been considered to be more efficient in undertaking simulations at high resolutions as required for this study than the explicit schemes of WAVEWATCH III®.

The following section provides a description of the SWAN model and the source functions. A brief description of the Lake George experiment and the field data used in this study is presented in Section 3. The numerical simulations using the SWAN model and the modelling results are discussed in Section 4 and the conclusions are summarized in Section 5.

2. SWAN model

SWAN is a third-generation phase-averaged model. The evolution of the wave spectrum is described by means of the radiative transfer

equation, which in shallow water can be written as

$$\frac{\partial N}{\partial t} + \nabla . cN = \frac{S_{tot}}{\sigma} = \frac{S_{in} + S_{ds} + + S_{nl} + S_{bot} + S_{db} + S_{tr}}{\sigma} \quad (1)$$

where $N = N(\sigma, \theta, x, t)$ is the wave action density spectrum dependent on angular frequency $\sigma = 2\pi f$ from a frame of reference relative to any local currents, wave direction θ, distance vector x, and time t; f is the frequency; c is the energy propagation velocity of the waves in each dimension; S_{tot} represents all energy fluxes contributing to wind-wave evolution; and the action density is related to the energy density as simply $N = E/\sigma$. In deep water, it is generally accepted that wind-wave growth is primarily a result of three physical processes: atmospheric input from the wind to the waves S_{in}, wave dissipation (resulting from breaking and interaction with turbulence and viscosity) S_{ds}, and nonlinear energy transfer between the wave components S_{nl}. In finite-depths, additional terms resulting from the bottom-friction S_{bot}, depth-induced breaking S_{db}, and triad interactions S_{tr} may become significant. The extent of the influence of these terms will depend on the environmental and site-specific conditions. More terms such as those from reflection of waves from shorelines and coastal structures or wave attenuation due to ice can be formulated in relevance with particular circumstances. All of these source terms are spectral functions. The formulations for the source terms relevant to this study are described below.

2.1. Wind input term

The initial estimate for the wind-input term S_{in} in the ST6 model is based on Donelan et al. (2006) that represents young wind-waves to mature sea conditions. It has been modified and implemented in the SWAN model by Rogers et al. (2012). An additional term for negative input due to oblique and adverse winds was added to another, similar model (WAVEWATCH III) (Zieger et al., 2015) and subsequently included in SWAN (unpublished work by Dr. Y. Fan, Naval Research Laboratory). The modified S_{in} with the added negative input has been used in this study. The new terms include: (i) a physical constraint applied to the total stress; (ii) altered drag coefficient with a new formula; and (iii) spectral saturation expressed in terms of wavenumber rather than wave frequency, and (iv) negative input. The directional distribution, W is implemented as the sum of W_1 and W_2 such that the spectral partitions W_1 and W_2 complement one another. W is given by:

$$W(f, \theta) = W_1(f, \theta) - a_o W_2(f, \theta) \quad (2)$$

W_1 and W_2 are given by:

$$W_1(f, \theta) = \{\max[0,\ U_{10}/C \cdot \cos(\theta_{wv} - \theta_{wn}) - 1]\}^2 \quad (3)$$

$$W_2(f, \theta) = \{\min[0,\ U_{10}/C \cdot \cos(\theta_{wv} - \theta_{wn}) - 1]\}^2 \quad (4)$$

where θ_{wv} and θ_{wn} are the wave and wind directions, respectively, C is the phase velocity and U_{10} is the wind speed at an elevation of 10 m. W_1 represents following winds (waves and wind are in the same direction) while W_2 represents adverse wind conditions when there is a significant difference in the direction of winds and waves. For adverse winds, the growth rate is negative and taken as a fraction (a_o) of the growth rate of the following winds. The value of a_o is generally taken as 40% following laboratory observations from Donelan (1999). However, it is a tuning parameter in the parameterization of the wind input.

The momentum flux between the atmosphere and the ocean is determined by the wind stress. The total stress at the surface is taken to be the sum of wave induced turbulent stress and the viscous stress. A constraint on the computed normal stress is applied, which is that the normal stress may not exceed the total stress less the viscous stress. For calculations of normal and total stress and the wind input computations, the reader is referred to Rogers et al. (2012), though it is now modified to calculate the wave-supported stress using a vector integral rather than scalar integral (see also Zieger et al., 2015).

2.2. Whitecapping dissipation

The observation-consistent whitecapping term S_{ds} has been implemented by Rogers et al. (2012) in the SWAN model. It was proposed by Banner et al. (2000), Babanin et al. (2001), and Young and Babanin (2006). It has two key features: the first is that waves do not break unless the spectral density at that frequency exceeds a threshold spectral density calculated from the spectral saturation spectrum (Banner et al., 2000; Babanin et al., 2001). The saturation spectrum is defined by Phillips (1984). In terms of frequency spectra, the threshold spectral density is calculated as:

$$E_T(f) = \frac{2\,\pi B_{nt}}{A(f) C_g k^3} \quad (5)$$

where B_{nt} is an empirical constant following the investigation of wave-breaking probabilities by Babanin et al. (2007), $\sqrt{B_{nt}} = 0.035$. Once this threshold is exceeded, the dissipation depends critically upon the level of exceedance: $\Delta(f) = E(f) - E_T(f)$. The second key feature of the whitecapping term is that it is two phase, because it has been hypothesized to be separable into two distinct mechanisms (Young and Babanin, 2006a); thus, there are two separate dissipation terms:

$$S_{ds}(f, \theta) = [T_1(f, \theta) + T_2(f, \theta)] E(f, \theta) \quad (6)$$

$$T_1(f, \theta) = a_1 \gamma_1^{p1} \quad (7)$$

$$T_2(f, \theta) = a_2 \left(\int_{f'}^{f} \gamma_2^{p2} df' \right) \quad (8)$$

$$\gamma_1 = \frac{\Delta(f)}{\tilde{E}(f)}, \gamma_2 = \frac{\Delta(f')}{\tilde{E}(f')} \quad (9)$$

The first dissipation mechanism is the inherent breaking component T_1, which accounts for breaking resulting from instabilities of waves at that frequency. The second breaking component T_2 is a cumulative term and accounts for the dissipation of waves induced by the breaking of longer waves, for example, via turbulence created by such breaking events. The exceedance levels $\Delta(f)$ are normalized by spectral density $\tilde{E}(f)$.

Rogers et al. (2012) calibrated the dissipation terms using single point model simulations and proposed four sets of coefficients, a_1, a_2, p_1 and p_2. These four coefficients result in different shapes of the dissipation terms, T_1 and T_2. As part of the calibration, two coefficients (a_1 and a_2) were found that yield the best match of the total energy in idealized duration-limited tests to two pre-existing models, including the default physics of SWAN. The relative size of a_1 and a_2 is set to achieve a desired ratio of T_1 and T_2 at large wave age values at moderate wind speeds.

The power coefficients p_1 and p_2 control how strongly the dissipation term reacts to the threshold exceedance. The dissipation becomes large when p_1 and p_2 are greater than 1 because this leads to increase in the exceedance $\Delta(f)$. Increasing the values of p_1 and p_2 to even larger values of 4 and 8 suggest an explosive increase in the dissipation. However, this is considered to be physically more realistic in situations where the wave energy must diminish within a small time or spatial scale due to wave blocking (Rogers et al., 2012) or due to sudden wind turns.

In this study, we use slightly different values of coefficients than those of Rogers et al. (2012). The updated coefficients were determined using the methods of Rogers et al. (2012) but accommodate recent updates to that physics package, such as non-breaking swell

dissipation, negative input in the parameterization for the wind input, and the vector form of the wave supported stress calculation.

2.3. Swell or nonbreaking dissipation

The new whitecapping dissipation formulation S_{ds} represents the rapid dissipation from breaking waves. At low wind speeds and in the absence of whitecapping, other mechanisms of wave dissipation become important.

In a decaying wind-sea situation, once the spectral density at any frequency falls below the breaking threshold E_T, it can no longer be dissipated via the whitecapping dissipation term S_{ds}. This is of particular importance in context of swell energy, which is known to attenuate slowly (Collard et al., 2009; Ardhuin et al., 2009; Young et al., 2013). If this dissipation is not included in global models with the threshold-based dissipation, this leads to over-prediction of swells, most noticeable as a positive bias in wave height in the tropics. It is therefore necessary to include the relatively slow dissipation of nonbreaking waves. Babanin et al. (2011), Young et al. (2013) and subsequently Zieger et al. (2015) parameterized the swell dissipation in the form of production of turbulence by waves. Following the Zieger implementation in WAVEWATCH III® (Tolman, 2014), the formulation for swell or nonbreaking dissipation, S_{nb} has been implemented in SWAN (unpublished work by Dr. Y. Fan, Naval Research Laboratory) as:

$$S_{nb}(\sigma,\theta) = -2/3 b_1 \sigma \sqrt{B_n} \cdot E \cdot (\sigma,\theta) \tag{10}$$

where b_1 is the non-dimensional proportionality coefficient. Young et al. (2013) estimated the bounds for b_1 to fall between 0.0002 and 0.0014 based on altimeter data. The upper bound of 0.0014 has been confirmed using a simple one-dimensional propagation test in SWAN. Ardhuin et al. (2012) and Zieger et al. (2015) showed that the value for b_1 obtained from observations does not yield satisfactory results in swell dominated regions such as the Central Western Pacific. Zieger et al. (2015) found that the model skill relative to altimeter estimates of wave height improved when scaling b_1 with wave steepness instead of using a constant value as shown below.

$$b_1 = B_1 2 \varepsilon k_p \tag{11}$$

where ε^2 is the total sea surface variance, k_p is the peak wave number, and B_1 is a scaling coefficient. For this study, we used a constant value of 0.0014 for b_1 based on confirmation from the model testing in SWAN mentioned above.

2.4. Bottom-friction dissipation

The SWAN model incorporates several different formulations for estimating dissipation due to bottom-friction. The following three models based on different physical processes were chosen for sensitivity testing:

(i) JONSWAP model with constant bottom-friction
(ii) Madsen model based on eddy-viscosity and roughness length
(iii) Smith model based on Smith et al. (2011) term for formation of ripples and initiation of sediment mobility
(iv) JONSWAP model

This is the simplest model; it is the default setting in the SWAN model. It was proposed by Hasselmann et al. (1973) and is given by:

$$C_b = \Gamma / g \tag{12}$$

where g is the acceleration due to gravity and Γ is the experimental value determined from the JONSWAP data. The most common value of Γ that has been known to perform well under many different conditions is 0.038 m^2/s^3. This is the default value of Γ in the SWAN model.

(i) Madsen model

Madsen et al. (1988) derived a bottom-friction formulation based on the eddy-viscosity concept:

$$C_b = \mathrm{f_w g U_{orb}} / \sqrt{2} \tag{13}$$

$$U_{\mathrm{orb}}^2 = \int_0^{2\pi} \int_0^{\infty} \frac{\sigma^2}{g^2 \sinh^2 kd} E(\sigma,\theta) \partial\sigma \, \partial\theta \tag{14}$$

where U_{orb} is the wave orbital velocity, f_w is the non-dimensional friction factor that depends on the roughness length, k_n. $E(\sigma,\theta) = \sigma\ N(\sigma,\theta)$ is the wave energy density, and θ is the wave direction. The SWAN model provides an option of using a constant value of k_n or linking it with Manning's n using Jonsson (1966) formulation.

(i) Smith model

Smith et al. (2011) implemented a new formulation for bottom-friction in the SWAN model that describes dissipation from the formation of sand ripples at the sea-bed. The model is based on the method of Nielsen (1981, 1992) and accounts for the sediment grain size in the absence of ripples and for ripples when ripples are formed. The friction factor, f_w, is given by:

$$f_w = \exp\left(5.213\left(\frac{k_s}{A_b}\right)0.194 - 5.977\right) \tag{15}$$

where k_s is the Nikuradse roughness coefficient and A_b is the near-bottom amplitude excursion. The ripples are only formed when the sediment is mobile on the seabed. The threshold of sediment movement is given by Shield's parameter:

$$\theta_s = \frac{U_{orb}^2}{(S-1)gD} \tag{16}$$

where U_{orb} is the wave orbital velocity, S is the specific gravity of sediment, and D is the median sediment diameter. It is generally accepted that sediment will become mobile when θ_s exceeds 0.05. When θ_s exceeds 1, 'sheet flow' is generated and the ripples are 'flattened'. The initiation of sediment movement is defined in three distinct stages based on the exceedance of θ_s against specific threshold criteria: (1) sediment immobility, when θ_s is less than 0.05; (2) initiation of sediment movement when $0.05 < \theta_s < 1$; and (3) sheet flow when $\theta_s > 1$. The Smith model computes a different roughness coefficient for each one of the three stages. If the sediment is not mobile, then ripples are not formed (stage 1) and the roughness coefficient is calculated on the basis of grain size as:

$$k_s = 2.5D \tag{17}$$

Otherwise (18) is applied to compute the roughness coefficient.

$$k_s = \frac{8\eta^2}{\lambda} + 170D(\theta_s - 0.05)^{0.5} \tag{18}$$

where η is the ripple height and λ is the ripple wave length from Nielsen (1981).

Smith et al. (2011) validated their model based on roughness coefficients estimated from the model against laboratory measurements of roughness coefficients using Lake George sediment in a broad range of conditions, including ripple formation and erosion (Babanin et al. 2005). Direct grain size measurements were not available, therefore, Smith et al. (2011) calculated sediment diameters using formulations that related roughness coefficients to sediment sizes. It was found that the sediment sizes ranged from clay-sized particles to fine sand with a median diameter of 0.1 mm. The new friction subroutine improved the accuracy of the wave model for Lake George applications.

2.5. Nonlinear interactions

It is widely accepted that nonlinear four-wave interactions (quadruplets) play a key role in wind wave evolution (Young and Van Vledder, 1993). The ocean waves can be considered as a superposition of independent spectral components at the first order while at the higher order, there is an interaction between spectral components resulting in exchange of energy between components (Hasselmann 1962, 1963). The nonlinear energy transfer conserves both the total energy and the momentum of the wave field.

The SWAN model uses the two methods mentioned in Section 1 for solving the nonlinear term, the XNL and the DIA.

The XNL is based on the Boltzmann integral formulation (SWAN Team, 2014). This is similar in expression to that used in theoretical physics to describe the rate of change in particle density distributions in a system of interacting particles (Young, 1999). The Boltzmann integral describes the rate of change of action density of a particular wave number due to resonant interactions between pairs of four wave numbers. To interact these wave numbers must satisfy the following resonance conditions:

$$k_1 + k_2 = k_3 + k_4 \tag{19}$$

$$\sigma_1 + \sigma_2 = \sigma_3 + \sigma_4 \tag{20}$$

where k is the wave number and σ is the angular frequency. The resonance conditions define not only the frequencies of the spectral components but also their propagation directions. Hence all components of the spectrum are potentially coupled and energy can be exchanged between components of different frequency as well as different directions. The XNL computes a full grid of possible wave interactions as exact as possible. Not all possible interactions are considered, only those with a high energy content. The details of the computation of XNL are given in van Vledder (2006).

The DIA method as proposed by Hasselmann et al. (1985) is relatively crude in its approximation of the Boltzmann integral. In the DIA, two quadruplet wave number configurations are considered, both with frequencies:

$$\sigma 1 = \sigma 2 = \sigma, \quad \sigma 3 = \sigma(1+\lambda) = \sigma+, \quad \sigma 4 = \sigma(1-\lambda) = \sigma- \tag{21}$$

where λ is a coefficient with a default value of 0.25. Within this discrete interaction approximation, the source term $S_{nl}(f,\theta)$ for the nonlinear transfer rate is given by (SWAN Team, 2014):

$$S_{nl}(f,\theta) = S^{*}_{nl}(f,\theta) + S^{**}_{nl}(f,\theta) \tag{22}$$

where S^{*}_{nl} refers to the first quadruplet and S^{**}_{nl} refers to the second quadruplet. Whilst the DIA reproduces the basic properties of the nonlinear interactions, the neglect of so many possible interactions has consequences, for example, it does not resolve the details of the spectrum like peakedness and directional spreading. The deficiencies of DIA become more apparent in complex situations, such as rapid wind shifts, slanting fetch, and mixed seas (Young and van Vledder, 1993).

When compared with other source terms, S_{nl} is flexible and can change its shape dramatically with spectral growth while for S_{in} and $S_{ds,}$ the change shape with spectral evolution is less dramatic. Thus a very different source term balance at different stages of the spectral development is achieved (Young and van Vledder, 1993).

3. Lake George experiment

The field data used in this study has been collected during the Australian Shallow Water Experiment (AUSWEX) (Young et al., 2005). The experimental site is located at Lake George in South-eastern Australia. The length of the lake is 25 km and the maximum width is 12.5 km with a relatively uniform water depth of approximately 2 m (bottom slope of the order of ~0.001). Therefore, the waves develop in a bottom-limited environment and long waves never grow. Typical Lake George wave spectrum has peak waves in finite depths and the spectrum tail in deep water (see e.g. Babanin and Makin, 2008). The lake bed consists of fine-grained silt laid down over many thousands of years (Young and Babanin, 2006b). The wind blows mainly perpendicular to the shoreline and the wind speed across the length and width of the lake is almost uniform with variations less than 1 m/s (Young and Verhagen, 1996). The field campaign at Lake George is unique in terms of the size and configuration of the lake, and thus provided an ideal site for fetch-limited finite-depth wave measurements. The lake site is essentially like a large laboratory that is forced with natural mechanisms for wind-wave generation.

Although the field campaigns at Lake George spanned over a period of approximately 3 years during different field campaigns in 1992–1994 and 1997–2000, the data used in this paper are limited to the data extracted for two specific wind turning events on 27 October 1997 and 31 October 1997 from the comprehensive data set.

The measurements of 1992–1993 (Young and Verhagen, 1996) consisted of collecting data from eight different locations that were oriented in a North-south direction. The data from these measurements indicated that the predominant direction of the wind was from the West and North-west. Easterly directions were also found to be common but the northerly and southerly winds were rare. Based on this knowledge, a new measurement site on the eastern coast of the lake was chosen for the 1997–2000 field campaign. At this location, the wind predominantly blew perpendicular to the shoreline, thereby minimizing the slanting fetch conditions. The aim was to avoid asymmetry that may arise from slanting fetch and to keep the conditions as simple as possible, and as close to ideal as possible. A maximum fetch of approximately 8–10 km was available for westerly winds at the experimental site. During this campaign data were collected at the new experimental site only. The observation sites from the 1992–1993 campaign had been decommissioned.

The experimental site consisted of a shore-connected platform located approximately 50 m offshore that was accessible via an elevated walkway. The measurements were made midway along a 10 m long measurement bridge extending from the side of the platform. The water surface elevation was measured by an array of capacitance wave probes deployed at the edge of a pier in approximately 1 m depth. This provided directional wave information, detection of wave breaking events, and the mean position of the water surface. The wave probes had an accuracy of 0.4% and a 2 ms response time. The output voltage measured by the wave probes is directly proportional to the surface elevations. The probes were calibrated in the laboratory prior to deployment. The calibration procedure provided a simple linear relationship between the voltage and the wave height to convert voltages into wave heights. The sampling rate of the wave probes was 25 Hz with individual records of 20-min duration (30,000 samples). These records were processed to obtain one-dimensional and two-dimensional spectra and the integrated parameters. The two-dimensional spectra were computed using the maximum likelihood method.

An anemometer mast with wind probes at 10 m and 5.65 m and a direction vane at 10 m above the water surface was erected at the end of the measurement bridge to avoid disturbing the airflow. The wind speed, U_{10} and wind directions measured very close to the 10 m above the water level were used for this study. The wind probes consisted of wind speed and wind direction sensors manufactured by Aanderaa Instruments. The wind speed sensor had a threshold speed of less than 0.4 m/s, with an accuracy of ±2% or ±0.2 m/s (greater of the two). The wind direction vane had a threshold speed of 0.3 m/s and an accuracy of ±5°. The sensor outputs consisted of 1 min average values.

All measurements were synchronized. Relatively young, strongly forced waves with U_{10}/c_p in the range of 3.5–6.5 (c_p is the phase speed) were observed. Under typical meteorological conditions, the range of values of the non-dimensional depth kd were found to be $0.7 < kd < 3.5$ (Young and Babanin, 2006b; Babanin et al. 2001) where, k is the wave number, and d is the water depth. The dataset can be categorized as spanning over the 'transitional water depth region' assuming that $kd > \pi$ for deep water and $kd < \pi/10$ for shallow water. The details of the field program are provided in Babanin et al. (2001, 2007).

4. Numerical simulations

Two separate events when the wind suddenly changed direction within 1 min during the AUSWEX field campaign at Lake George were identified and selected for undertaking numerical simulations. The two events are: (1) wind turning by 180° on 28 October 1997 16:19; and (2) wind turning by 90° on 31 October 1997 17:58.

The synchronized measurements of wind and waves were available approximately 1 h before and 1 h after the wind changed directions, therefore the duration of the numerical simulations was restricted within this timeframe. The wind data was used as input for the model while the wave data were used for model validation.

For both the 180° and 90° cases, the wind direction was fairly constant before and after the wind turns. For the 180° turn, the wind was initially westerly (270–290°), then shifted to the opposite easterly direction (75–90°). Since the wave array is located on the eastern shore of Lake George, this case presented good conditions to test the wave response as a result of the sudden wind direction change from the West to the East and the associated reduction in fetch from about 10 km to approximately 50 m. Nevertheless it is rare to have ideal conditions in the field, thus the wind speed did not remain constant as would have been desirable but reduced from 5 m/s to a low speed of 1.5 m/s after which the wind turned by 180°. Thereafter the wind speed rapidly increased to a maximum of 10 m/s in the following 20 min.

The wind speed during the 90° case was higher than the 180° case. Immediately prior to the wind turning, the wind speed started increasing from 10 m/s to 15 m/s, then varied between 12 m/s and 20 m/s over the following half-hour after the wind turn. The wind direction changed from approximately North-north-westerly to West-south-west.

The measured wind data from the Lake George field data set were re-processed to create a time-series of wind speed at 10 m and wind direction at 1 min intervals. The wind direction sensor measures the wind directions relative to magnetic North. These were converted to true North taking into account the magnetic deviation at the site at the time of the measurements. Since wind measurements were conducted only at one location during this field campaign, we had to make an assumption regarding the spatial distribution of the wind field. Measurements of wind speeds at eight different locations in Lake George show minor variations of wind speeds across the North-south axis of the lake (Young and Verhagen, 1996). On this basis, we assumed a spatially uniform distribution, and applied the time-varying winds uniformly over the entire model domain as the forcing field for the SWAN model. Given the small size of the lake, this appears to be a reasonable and less intrusive assumption in comparison with that of any variable spatial distribution. However, to test the validity of the assumption of spatially uniform wind fields, we have conducted extensive sensitivity testing using assumed spatially varying wind fields and simulation of fronts moving across the lake. Details of the sensitivity testing are provided in Section 4.1.

A rectangular grid with a spatially varying grid size in both directions was developed. The grid size varied from 7 m × 10 m at the experimental site to approximately 250 m × 300 m along the outer boundaries of the model. The model grid covered the entire Lake George. Fig. 1 shows the model grid and bathymetry. The model grid is coarse away from the experimental site and progressively gets finer toward the study site as shown in the three plots. The fine spatial resolution is essential to capture the immediate directional wave response to turning winds at the experimental site at Lake George. It was evident from initial model testing that a model set-up with a grid spacing greater than 20–30 m in the vicinity of the experimental site was not able to reproduce observed changes in wave direction in response to sudden changes in wind direction. Since the observed wave lengths were on the order of few meters, a grid size comparable to the wave length was chosen for the finest grid around the measurement site.

Table 1
Summary of model simulations.

	Physics	Bottom-friction	Numerical scheme	Wind turn
1.	ST6	Smith	XNL	180°
2.	ST6	Smith	DIA	180°
3.	ST6	JONSWAP (0.038)	DIA	180°
4.	ST6	Madsen (0.05)	DIA	180°
5.	Komen	JONSWAP (0.038)	DIA	180°
6.	ST6	Smith	XNL	90°
7.	ST6	Smith	DIA	90°
8.	ST6	JONSWAP (0.038)	DIA	90°
9.	ST6	Madsen (0.05)	DIA	90°
10.	Komen	JONSWAP (0.038)	DIA	90°

Given that the wind input time-series varies over a time-interval of 60 s, a model time-step of 30 s was chosen to run the SWAN model in a non-stationary mode. The simulations were conducted using the MPI protocol that enables parallel computing on multiple processors of the high performance computing (HPC) machine. The spectral grid consisted of 45 frequencies in the range of 0.11–12 Hz. The upper frequency limit was chosen such that $f_{max} > 6f_p$, which is recommended (SWAN Team, 2014) when using the XNL model. It is also close to the upper frequency adopted when undertaking spectral analysis of the recorded wave data. The SWAN model uses a logarithmic distribution for the frequencies such that the frequency interval $\Delta f = 0.1$ f. The directional interval was chosen as 10°. While the spectral grid was the same for both the DIA and XNL runs, the computational domain was de-refined by an approximate factor of 2 for the XNL model. This was done to improve computational efficiency.

Following Smith et al. (2011), the sediment diameter was chosen as 0.1 mm (100 μm) for this study. This represents very fine sands. Initial testing using median diameters that represented silt fractions (60–70 μm) indicated minor sensitivity within the size range of 60–100 μm.

The numerical simulations have been conducted with a test version of SWAN that consists of the new source terms of the ST6 model (Rogers et al, 2012). The new bottom friction term (Smith et al., 2011) henceforth referred as the 'Smith' model was added in this test version of the SWAN model. The Smith model has been implemented in the SWAN version 41.01. The modelling employed both the DIA from Hasselmann et al. (1985) and XNL from van Vledder (2006).

The aim of this study is to evaluate the new physics (ST6) in comparison with the existing default physics of the SWAN model, therefore simulations with the default physics (Komen et al., 1984, 1994) of the SWAN model in combination with the default friction model (JONSWAP), henceforth referred to as the 'Komen/JONSWAP' model were conducted.

The location of the study site in close proximity to the shoreline means that the bottom-friction will have a strong influence on the wave dissipation and growth. Therefore, three additional models for bottom-friction were assessed in combination with the ST6 physics: (1) Smith (Smith et al., 2011); (2) JONSWAP; and (3) Madsen (Madsen et al., 1988). A summary of the model simulations is given in Table 1.

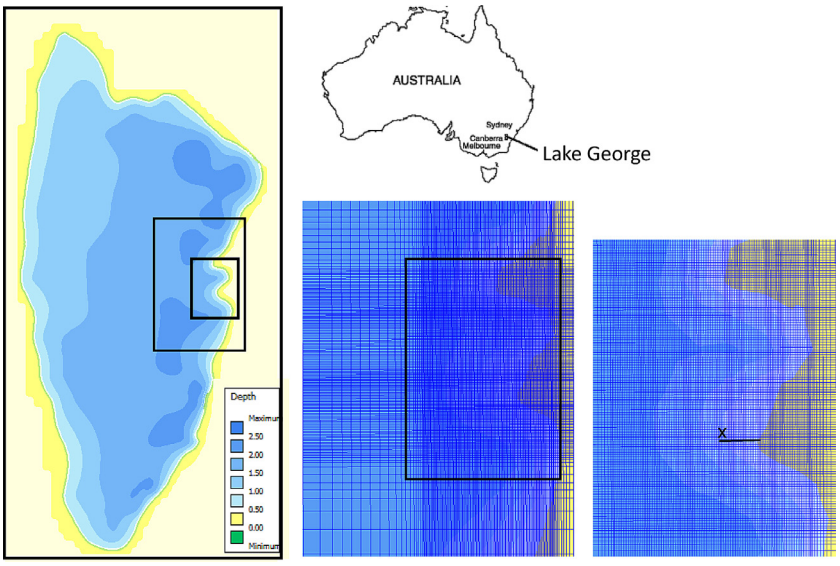

Fig. 1. Lake George model grid and bathymetry. The entire model grid extent is shown by the outer-most boxed area. The inner boxed areas indicate that the grid has been progressively refined in these areas, shown (and enlarged) in subsequent plots. 'X' represents the location of the experimental site.

4.1. Sensitivity analysis

We recognize that the wind speeds and wind directions are likely to vary across the body of the lake during sudden wind shifts. Therefore, to evaluate the validity of our assumption of spatially uniform wind fields, we performed sensitivity tests by applying spatially varying wind fields as model input. Two different methods were used to prepare the varying wind fields. The first method consisted of computing the variation of wind speed over the fetch by taking into account the land-sea boundary roughness (Taylor and Lee, 1984). Young and Verhagen (1996) have calibrated the Taylor and Lee formulation using the Lake George wind data. Their analysis shows that the wind increases sharply by up to 1 m/s during the initial 2–3 km of the North-south fetch at Lake George and thereafter, the increase in wind speed is very gradual becoming nearly constant near the downwind shoreline.

The data from the present study show similar increases in wind speed as those from Young and Verhagen (1996) of about 1 m/s at the upwind end due to the land-sea boundary layer. Such minor variations in wind speed may not be truly representative of wind conditions during sudden wind shifts. Therefore, a second method was employed where it was assumed that the passage of a front took approximately 30 min to move from the eastern to the western shores of Lake George. Further assumptions regarding the wind speed and the wind direction of the front have been made on the basis of observed data. The measured wind speeds and wind directions are applied at time t on the East while those at time $t+1$ are applied progressively to the West (changing in time and position). The wind changes direction at different times and at different locations as the front progresses. The front is moves at a speed of 5–6 m/s. Simulations using the ST6/Smith/DIA model were undertaken for the 180° wind turn event.

The resulting significant wave heights, peak wave periods, and wave directions at the experimental site (Fig. 2) from both methods described above show minor variations when compared to the results using spatially uniform winds. The predictions of the wave directions showed slight improvement against the observations when using spatially varying winds. Generally the differences in H_s between the two models are less than 0.01 m at the measurement site and less than 0.05 m across the lake about 10 min after the wind turn. Larger differences in H_s up to 0.1 m have been computed at the western end of the lake 25 min after the wind turn. These result from the differing wind fields as the front progresses toward the west. However at the measurements site, the variations in wave heights and wave directions are small.

Table 2
Sensitivity testing of SWAN model parameters.

Model parameter	Settings tested
p_1 and p_2	$p_1 = p_2 = 4$ and $p_1 = p_2 = 8$
b_1	0.0014, 0.004
Bottom-friction	Smith, Madsen, JONSWAP
Negative wind input, a_o	0.04, 0.4, 0.9

The sensitivity testing provided confidence that the local wind effects can be considered as being representative at the measurement site. The model is able to reproduce the observed wave conditions within the area where wind conditions are known using both spatially uniform and spatially varying wind fields.

Further sensitivity analysis was performed to assess the influence of various model parameters on the model performance. These parameters are listed in Table 2. The p_1 and p_2 are coefficients for the whitecapping source term from (7) and (8) respectively, described in Section 2.2, b_1 is the coefficient for swell dissipation due to non-breaking waves from (10), and a_o is the coefficient for negative input from (2).

In addition to the parameters listed in Table 2, we adopted the values of wave-breaking parameters, a_1 and a_2 from (7) and (8) as 6.24E−07 and 8.74E−06 respectively. The values of a_1 and a_2 are based on limited calibration with a single idealized test case, together with concepts of physical constraints (or target behaviours), taken from ideas of Babanin et al. (2005, 2010), Tsagareli et al. (2010), and others.

Preliminary model testing indicated that the higher value of 8 for p_1 and p_2 provided a significantly better agreement with the measured data than the value of 4, therefore the value of 8 was adopted for all subsequent simulations. Using 4 instead of 8 for p_1 and p_2 resulted in severe overestimation of H_s because of reduced dissipation.

The model performance was determined by computing the statistical parameters: bias, standard deviation, and root-mean-square error (RMSE) between the modelled significant wave heights (H_s)

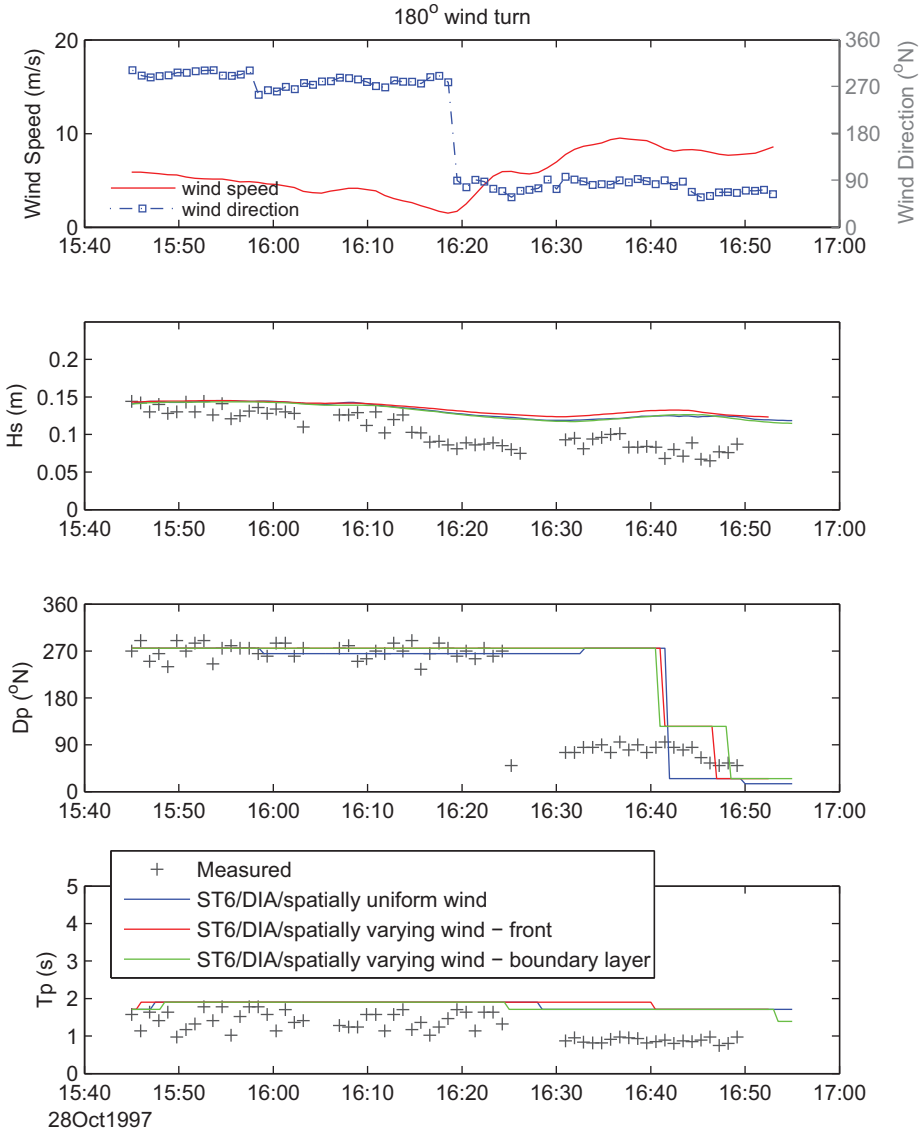

Fig. 2. Comparison of modelled wave parameters with field measurements at the experimental site using spatially uniform wind fields and spatially varying wind fields for the 180° wind turn event. Only the ST6/Smith/DIA model was tested.

extracted at the experimental site and the corresponding measured values of H_s. The bias is taken as the average of the difference between the modelled H_s and the observed H_s while the root-mean-square error (RMSE) is given by:

$$RMSE = \sqrt{\frac{1}{N}\sum_i \left(H_s\, model_i - H_s\, obs_i\right)^2} \tag{23}$$

Visual comparisons of one-dimensional and two-dimensional wave spectral output from the model before and after the wind turn were also done with the corresponding measured spectral data. The SWAN model results were further validated against the wave energy and frequency parameterizations of Young and Verhagen (1996), Young and Babanin (2006b), and Donelan et al. (1985).

4.2. Model results

Both the measurements and the output from the models have been analysed at high temporal (30 s) and (for the model) spatial resolutions (7–10 m) to capture the directional wave response to the sudden and rapid wind shifts. The model output has been extracted at 30 s and 60 s intervals for the integral parameters and the spectral parameters respectively. The wind and wave directions have been referred to as 'coming from' following the meteorological convention. The ST6 combined with the Smith bottom-friction reproduces the wave observations at the experimental site with good accuracy. The bias, standard deviation (STD), and root-mean-square error (RMSE) for H_s from the ten different simulations are presented in Table 3. A graphical comparison of modelled H_s, T_p (peak wave period), and D_p (peak wave direction) with the corresponding observed H_s, T_p, and D_p is shown in Fig. 3. The nomenclature used for the various model simulations is given in Table 3 under the column titled, 'Model Run'.

Table 3 indicates that the best model performance is achieved when using the ST6 physics. The bias and RMSE in H_s for the ST6/Smith/XNL simulation are the lowest while the worst-performance as indicated by a significantly large bias and RMSE is from the default Komen/JONSWAP/DIA model for both the 180° and 90° wind turn events. All ST6/DIA models show significantly better performance than the Komen/JONSWAP/DIA. Comparing the ST6/Smith/DIA model with the ST6/Madsen/DIA model shows that the Madsen formulation results in a smaller RMSE than the Smith model for the 180° case but has a significantly large bias, STD, and

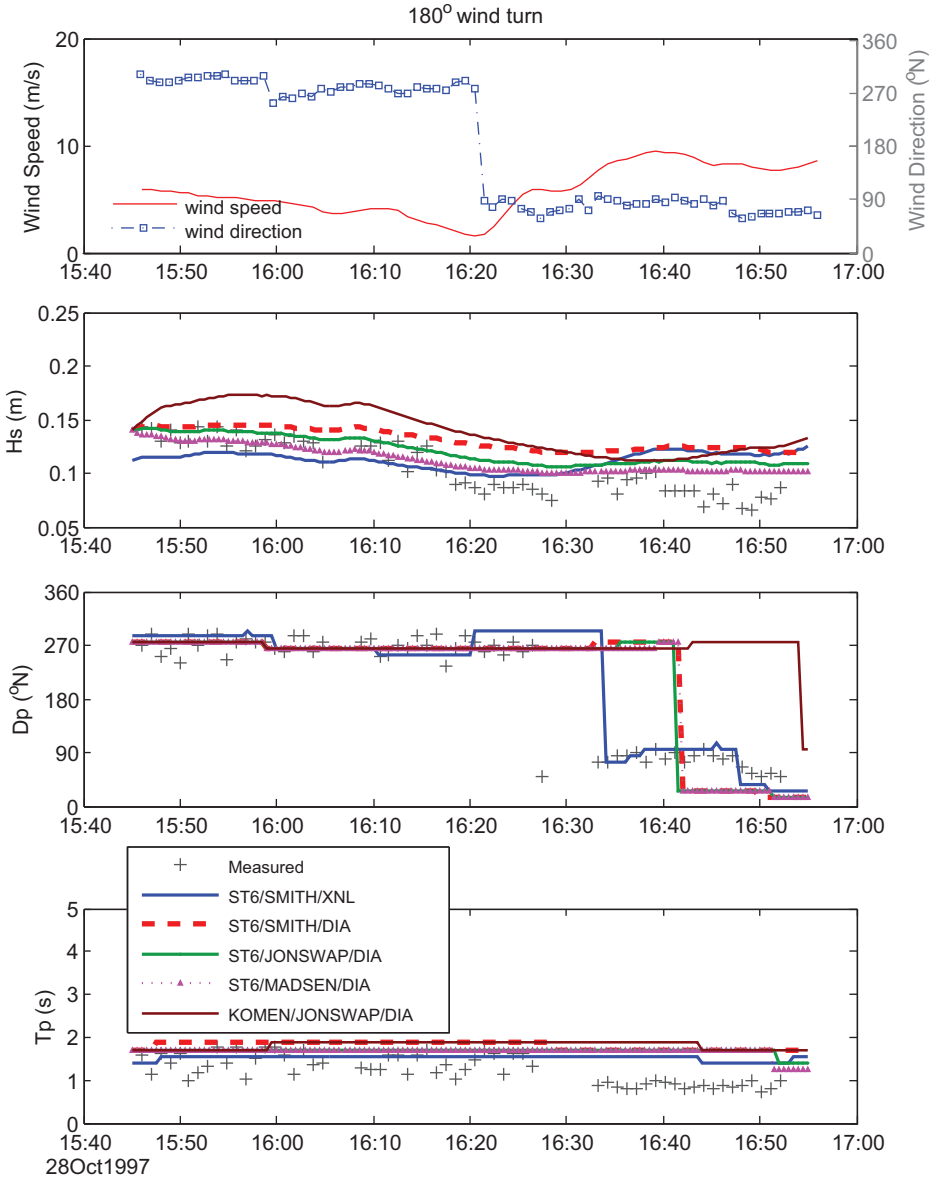

Fig. 3. Comparison of modelled wave parameters with field measurements at the experimental site for (a) 180° wind turn event; (b) 90° wind turn event.

Table 3
Median, bias, standard deviation (STD), and RMSE, in significant wave height, H_s (m).

Model run	Median H_s (m)	Bias	STD	RMSE
180° wind turn, median $H_s = 0.10$				
1. ST6/Smith/XNL	0.11	0.01	0.02	0.02
2. ST6/Smith/DIA	0.13	0.03	0.02	0.03
3. ST6/JONSWAP/DIA	0.11	0.02	0.01	0.02
4. ST6/Madsen/DIA	0.10	0.01	0.01	0.02
5. Komen/JONSWAP/DIA	0.14	0.04	0.01	0.04
90° wind turn, median $H_s = 0.21$				
6. ST6/Smith/XNL	0.24	−0.01	0.06	0.06
7. ST6/Smith/DIA	0.23	−0.02	0.07	0.07
8. ST6/JONSWAP/DIA	0.22	−0.02	0.07	0.07
9. ST6/Madsen/DIA	0.18	−0.04	0.06	0.07
10. Komen/JONSWAP/DIA	0.31	0.05	0.08	0.10

RMSE for the 90° case. The better performance of the Smith model in this case can be attributed to the ripples formation and the sheet flow that leads to stronger dissipation during high wind speeds. The impacts and features of the new source terms for dissipation and wind input in ST6 and the bottom-friction from the Smith model are discussed in Section 4.2.2 and Section 4.2.3.

Whilst the Komen/JONSWAP/DIA model overestimates the H_s in comparison with the ST6/Smith/DIA and ST6/Madsen/DIA models (Fig. 3), the main difference between the ST6/Smith/DIA and the Komen/JONSWAP/DIA models lies in the directional wave response. This is especially evident in the 180° event when the wind turns and blows in the opposite direction to the existing waves. Fig. 3a shows that when the wind changes direction by 180° at 16:19, the new (young) observed waves are generated that follow the direction of the shifted wind after approximately 10 min of the wind turn for ST6/Smith/XNL, 20 min for ST6/DIA models and 35 min for Komen/JONSWAP/DIA. The ST6/Smith/XNL lags behind the measurements by about 5 min. Among all the SWAN model simulations, the response time of ST6/Smith/XNL for generating new waves is closest to the observed data.

While the median H_s for the modelled 90° case is higher than the observed median for all models (except Model run #10 in Table 3), the model is biased toward an overall underestimation of H_s. The

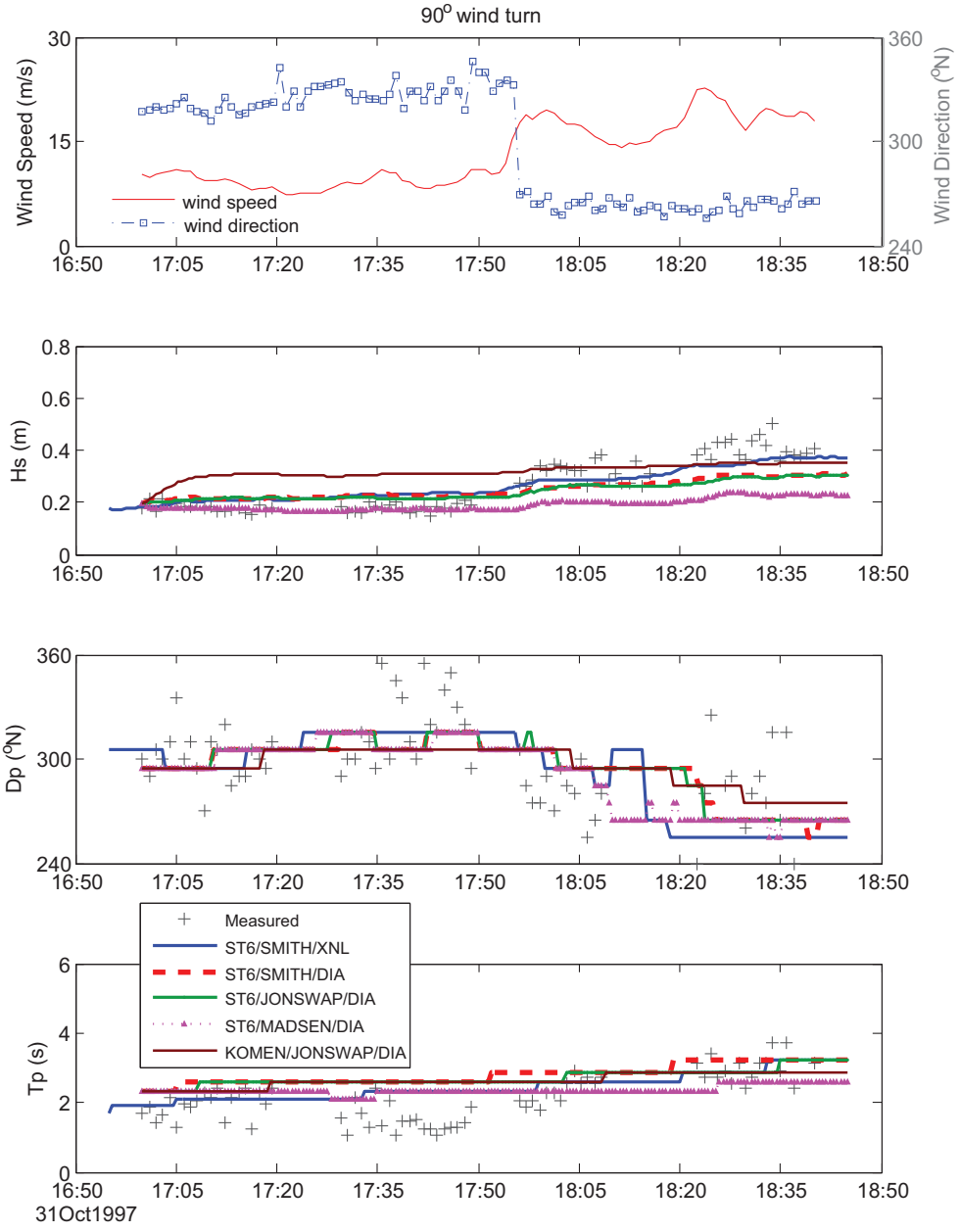

Fig. 3. Continued

reason for this is that the model severely underestimates the H_s after the wind turn and slightly overestimates the H_s before the wind turn, thus resulting in an overall negative bias.

The ST6/Smith/DIA shows a delayed directional response in comparison with the corresponding XNL model but the Komen/JONSWAP/DIA model takes the longest to respond to the wind shift. This is also evident in the two-dimensional wave spectra and is further discussed in Section 4.2.2.

The modelled H_s and T_p for all model simulations for the 180° case are in better agreement with the observed parameters before the wind turn. After the wind turn, the modelled H_s slightly overestimates the observed H_s for all model simulations. After the wind turn, the models are unable to reduce the T_p by the same magnitude as the observations. Given the complex situation of wind shifts and mixed seas, and the assumption of spatially uniform wind fields, the comparative statistics show that the model results (Table 3) are in good agreement with the observations.

In contrast with the 180° case, the modelled H_s for the 90° case (Fig. 3b) is generally underestimated by SWAN after the wind shift. The Komen/JONSWAP model shows the largest departures in H_s from the observations when compared with other models. The agreement between modelled and observed T_p is better after the 90° wind shift than before the wind turn. The ST6/Smith/XNL performs the best in predicting H_s in this case.

The differences in wave fields between the ST6/Smith/DIA and the Komen/JONSWAP/DIA models after 20 min of wind turning are presented in Fig. 4. While the H_s predicted by the ST6/Smith/DIA model is slightly higher by about 2–5 cm than the H_s from the Komen/JONSWAP/DIA across the model domain for the 180° wind event, the ST6/Smith/DIA produces significantly lower H_s than the Komen/JONSWAP/DIA model for the 90° wind turn (Fig. 4a,b, extreme left panels). There are pronounced differences in D_p between the two models (Fig. 4a,b, right panels) for both the 180° and 90° wind turns. The ST6/Smith/DIA model starts generating new waves in response

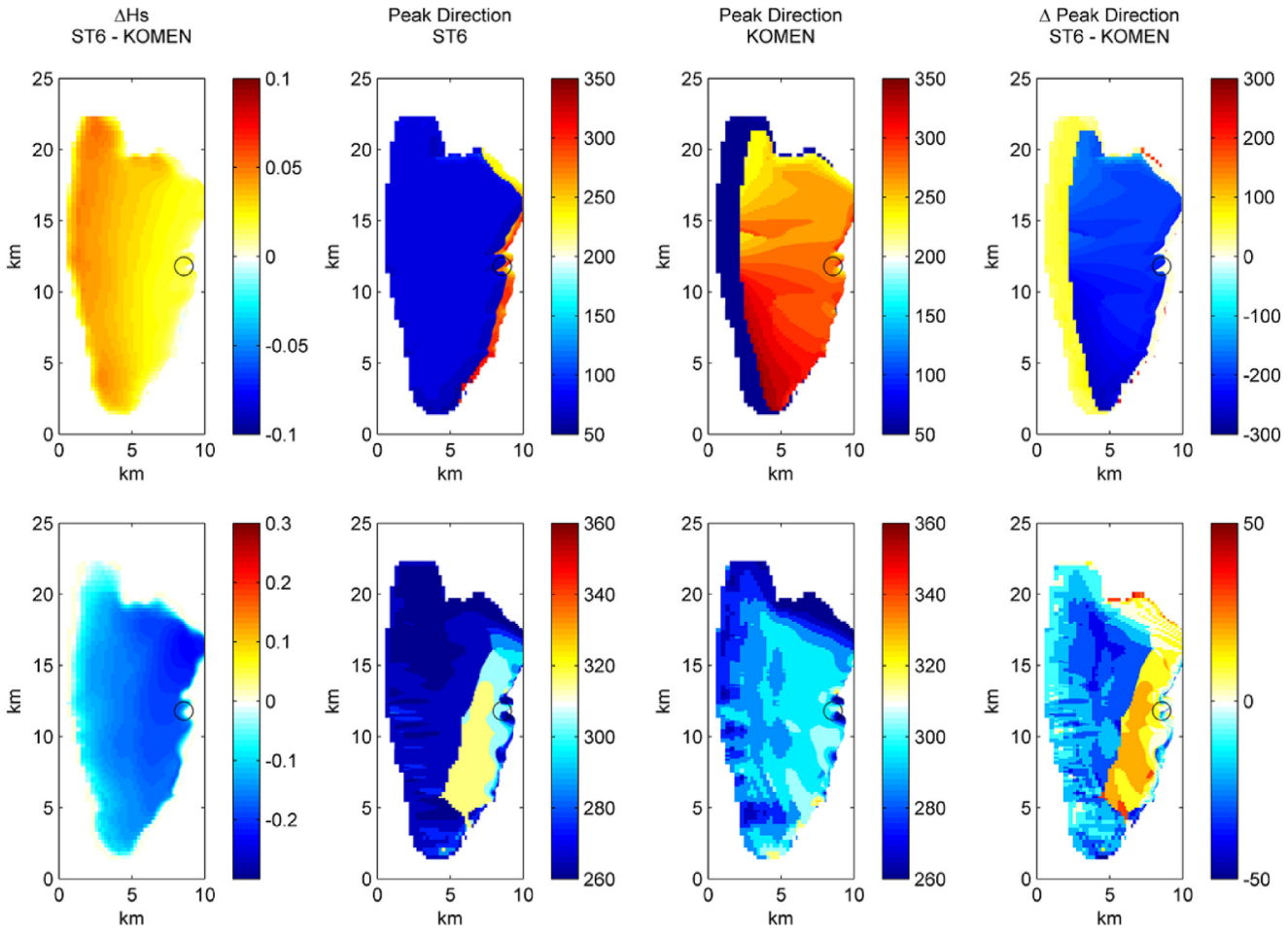

Fig. 4. Comparison of wave field maps for the ST6/Smith/DIA (ST6) and Komen/JONSWAP/DIA (Komen) models after 20 min of (a) 180° wind turn; and (b) 90° wind turn. The maps show the difference in H_s (m) between the ST6 and Komen models (extreme-left panels); peak wave direction D_p for ST6 and Komen models (middle panels); and the difference in D_p between the ST6 and Komen models (extreme-right panels). The circle represents the location of the experimental site.

to the 180° wind turn at a faster rate than the Komen/Smith/DIA model. After 20 min of the 180° wind turning, we see from Fig. 4a, that the new waves have been generated across nearly the entire model domain in the ST6/Smith/DIA model but are just about forming along a narrow boundary along the western shore in the Komen/JONSWAP/DIA model (Fig. 4a, middle panels). The differences in D_p for the 90° wind between the two models are less dramatic than the 180° wind turn. Nevertheless, there is a difference of nearly 25° between the ST6/Smith/DIA and the Komen/JONSWAP/DIA models at the experimental site (Fig. 4b, right panel).

In addition to the new wind input source term in the ST6, the dissipation source terms may also have an influence on the wave fields. In the Komen model, the main mechanism (other than bottom friction) for the waves to lose energy is via whitecapping while the ST6 includes dissipation via non-breaking turbulence and the negative wind input. This will be further discussed in Section 4.2.3.

There are minor differences between ST6/Smith/DIA, ST6/Madsen/DIA, and ST6/JONSWAP/DIA models where ST6 is combined with different bottom-friction models. Therefore the results from these models are presented and discussed in detail only when comparing dissipation from bottom-friction.

4.2.1. Validation

Integral growth curves expressed in terms of non-dimensional energy and non-dimensional frequency are generally used for assessment and calibration of wave models. Young and Verhagen (1996) used the full data set of 65,000 data points from the Lake George field campaign to refine the relationships developed by Bretshneider (1958) and Vincent and Hughes (1985) for depth-limited wave growth. They developed parametric forms for the fetch-limited growth of the non-dimensional energy ε, and non-dimensional frequency ν, as well as asymptotic depth-limited forms for ε and ν as functions of the non-dimensional depth, δ. The asymptotic values are represented by:

$$\varepsilon = 1.06 \times 10^{-3}\delta^{1.3} \tag{24}$$

$$\nu = 0.20\delta^{-0.375} \tag{25}$$

Young and Babanin (2006b) presented new asymptotic limits based on new measurements at Lake George where the data were recorded with a higher resolution wave probe with more refined measurements of the wind speed and under more closely observed environmental conditions than the previous field campaign. The slightly modified $\varepsilon-\delta$ relationship is given by:

$$\varepsilon = 1.06 \times 10^{-3}\delta^{1.2} \tag{26}$$

Instead of modifying $\nu-\delta$ relationship, Young and Babanin (2006b) found that the $kd-\delta$ relationship is more appropriate to represent the behaviour of the spectral peak. They determined the asymptotic limit to be:

$$kd = 1.80\delta^{-0.73} \tag{27}$$

The modelled results from this study are also evaluated against the relationship between peak frequency and wave energy for

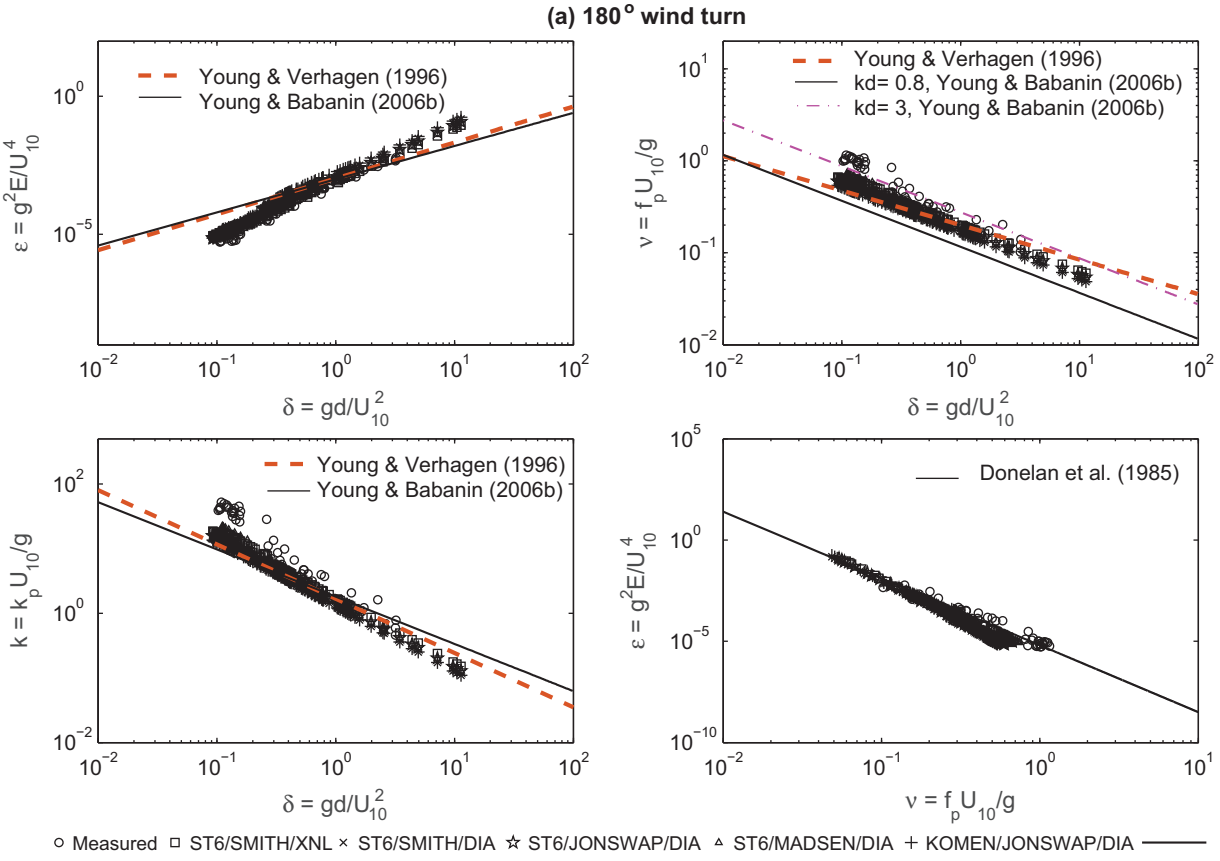

Fig. 5. Comparison of SWAN model results with Young and Verhagen (1996), Young and Babanin (2006b), and Donelan et al. (1985) for (a) 180° wind turn; (b) 90° wind turn.

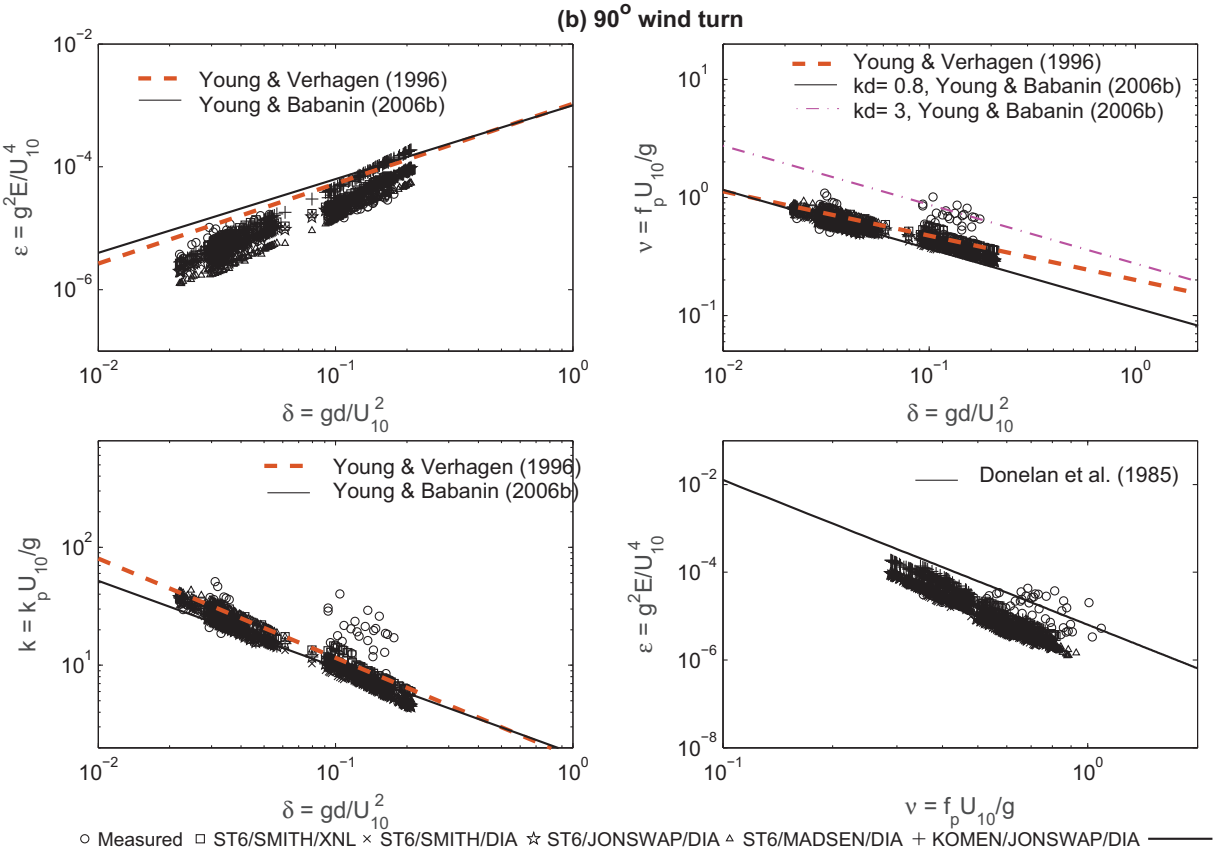

Fig. 5. Continued

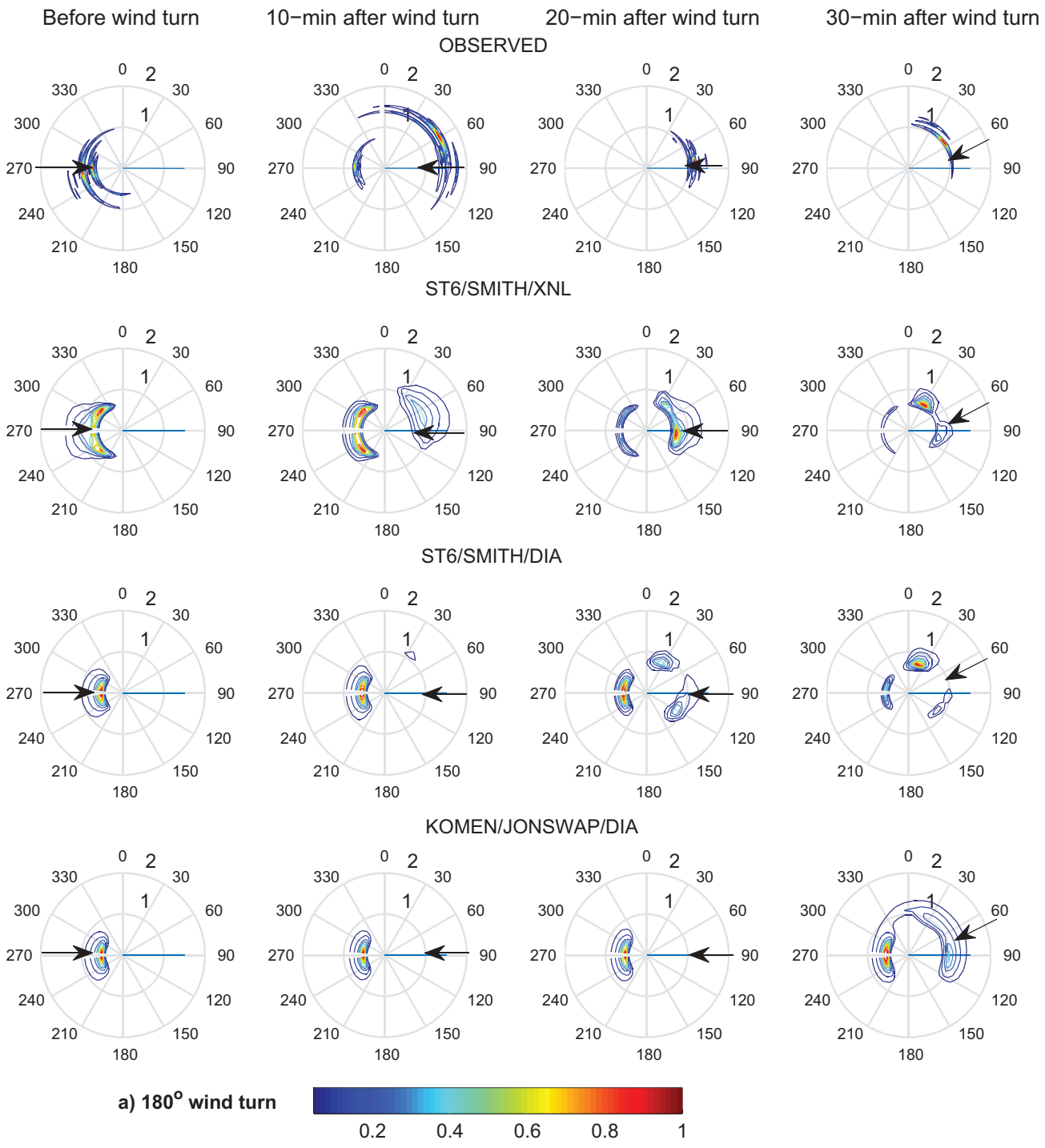

Fig. 6. The directional wave spectra for (a) 180° wind turn; (b) 90° wind turn. Black arrows indicate the wind direction. The spectra are scaled against the maximum value. The frequencies are represented by 1 Hz and 2 Hz at the inner and outer circles respectively. The gap along 270° is a result of the impreciseness of the plotting routine.

fetch-limited wave growth developed by Donelan et al. (1985). Their relationship was derived for simple unidirectional fetch cases and is similar to the formulas proposed by Hasselmann et al. (1973) for the JONSWAP dataset. The Donelan et al. (1985) formulation is given by:

$$\varepsilon = 3.635 \times 10^{-6} \nu^{-3.3} \tag{28}$$

The non-dimensional parameters are defined as $\varepsilon = g^2 E / {U_{10}}^4$, $\nu = f_p U_{10}/g$, $k = k_p U_{10}/g$, and $\delta = g d {U_{10}}^{-2}$ where E is the total energy of the spectrum, f_p is the peak frequency, k_p is the peak wave number, g is the acceleration due to gravity, d is the water depth, and U_{10} is the wind speed at an elevation of 10 m.

The ε, ν, kd, and δ have been computed using the model results and compared with the parameterizations in (24)–(28). The results from the SWAN model simulations along with the measured data for the two wind turning events are presented in Fig. 5.

Overall, the SWAN data are consistent with the parameterizations presented in (24)–(28). The different models are also in good agreement with each other. The strong dependence of the peak frequency on H_s (energy) for the 180° event is evident from the close agreement

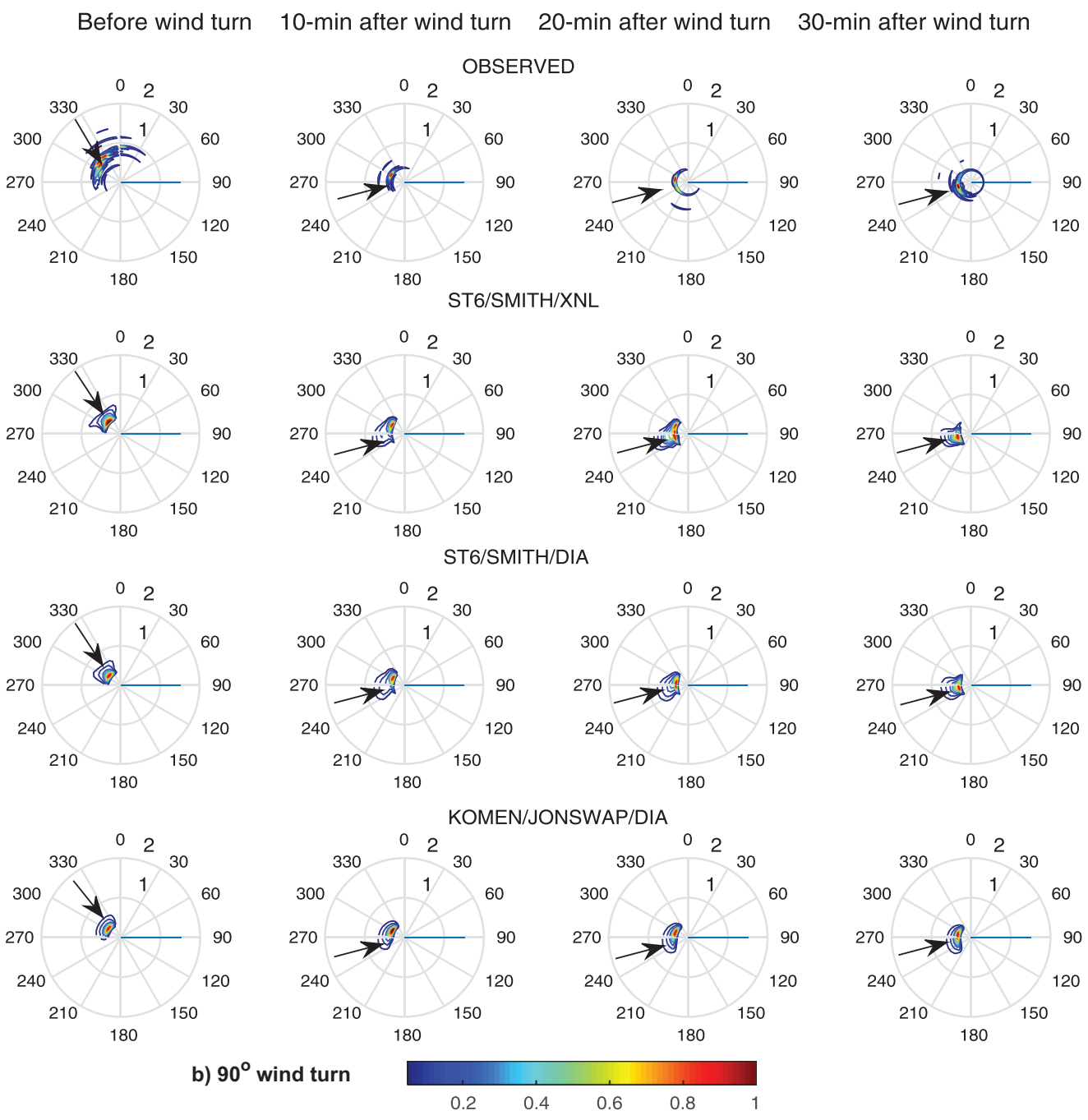

Fig. 6. Continued

of modelled ε vs. ν with the relationship given in (28). There are some data points that fall outside the asymptotic limits (Fig. 5a). These data correspond mainly to the easterly wind directions, which were excluded from the parameterizations.

The modelled ε and ν show better agreement with (24) and (25) when δ is in the range of 0.3–1 for the 180° case. As the model data are extracted at a single constant depth (0.95 m during the 180° event and 1.1 m for the 90° event), this corresponds to a U_{10} of 5–6 m/s, which is the dominant wind speed for the 180° event. For the 90° case (Fig. 5b), the best agreement between the modelled data and (24) and (25) is for smaller values of δ (0.03–0.1), which corresponds to the higher wind speeds of 10–18 m/s that occurred during this event.

4.2.2. Evolution of two-dimensional spectra

Evolution of the directional wave spectrum for the 180° and 90° wind shifts is shown in Fig. 6 for the modelled and measured data. As expected, there are minor differences between the various models presented before the wind turn but after the wind turn, the ST6/Smith/XNL solution shows a faster and more realistic wave directional response to the turning winds in comparison with the DIA models. The ST6/Smith/XNL starts developing young waves in the new wind direction within 5 min of the wind turn (not shown) while the peak energy appears in direction of the wind approximately 10 min after the wind shift. The ST6/Smith/XNL reproduces the timing and the spectral structure of the two wave systems in reasonable agreement with the measured spectra.

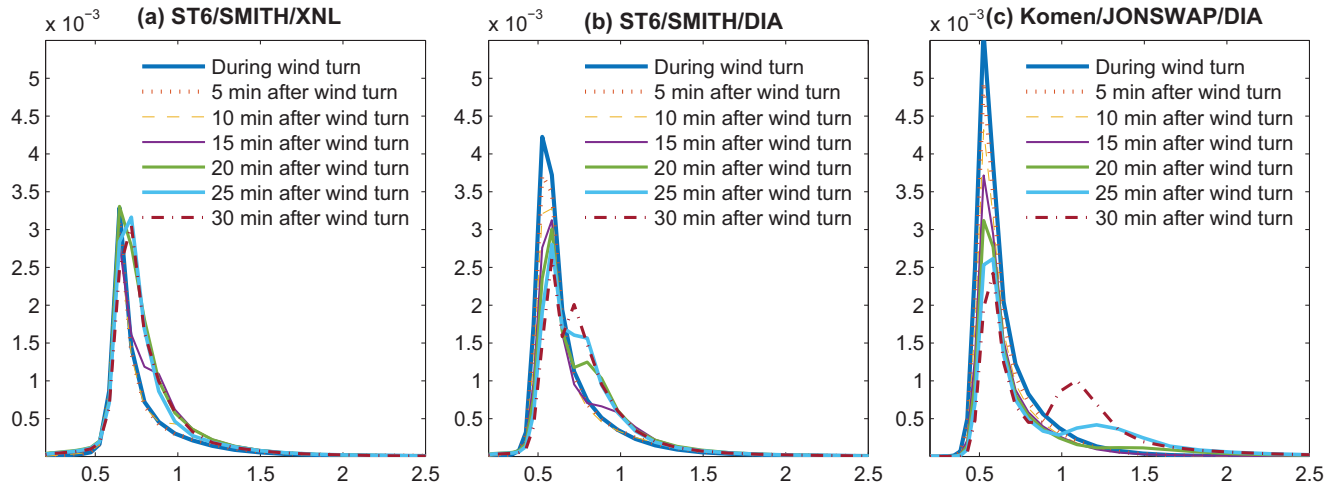

Fig. 7. Evolution of modelled one-dimensional spectra for (a) ST6/Smith/XNL; (b) ST6/Smith/DIA; and (c) Komen/JONSWAP/DIA models at intervals of 5 min after the 180° wind turn.

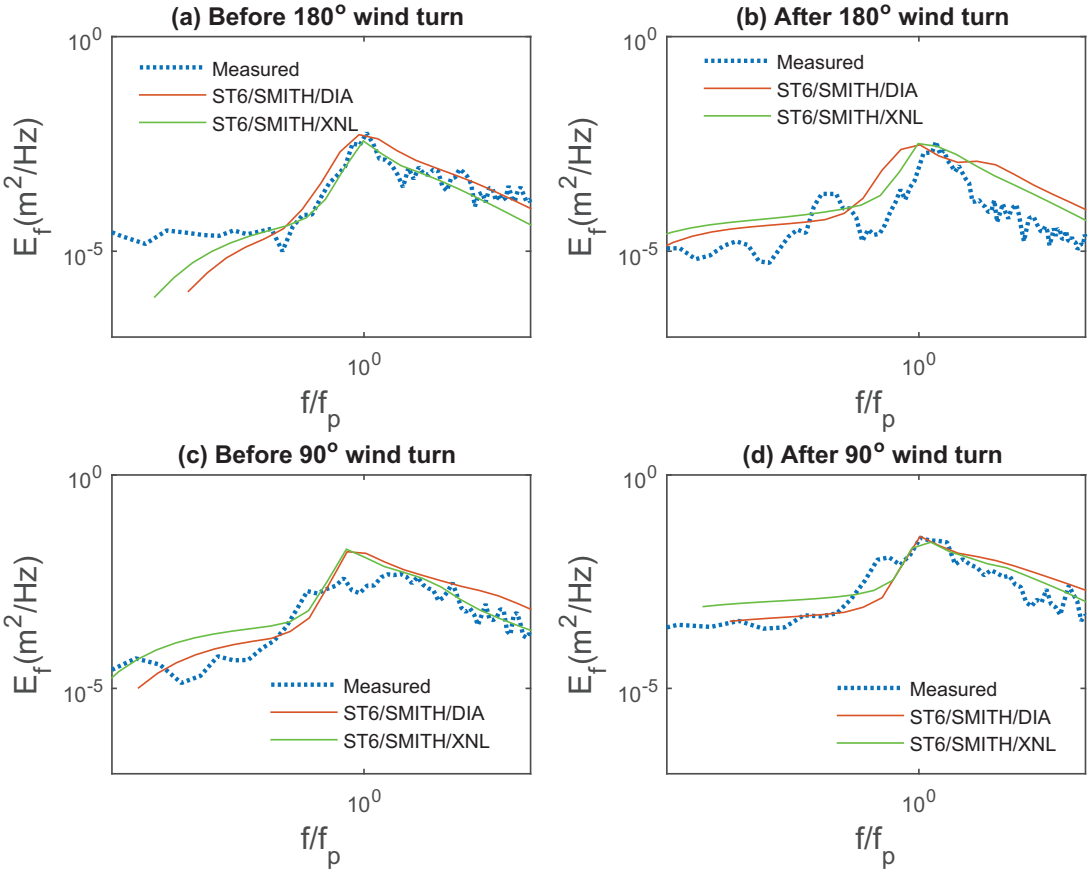

Fig. 8. Evolution of measured and modelled one-dimensional spectra for (a) 10 min before the 180° wind turn event; (b) 20 min after the 180° wind turn event; (c) 10 min before the 90° wind turn event; (d) 20 min after the 90° wind turn event.

Before the 180° wind turn, the dominant wave direction is westerly shown by the concentration of energy in the western sector for both the modelled (ST6) and the measured spectra (Fig. 6a). After 10 min of wind turning, the measured spectra has de-coupled into the 'old' sea and the 'young' sea. There is a secondary peak growing in the newly generated young sea. The ST6/Smith/XNL follows the measurements and starts generating wave energy (young wind-sea) in the North-easterly direction following the new wind direction while the ST6/Smith/DIA model still has the wave energy concentrated in the old wave system in the western sector. After 20 min, the measured spectra has fully decoupled and rotated to the new easterly direction. The old waves have completely decayed. The ST6/Smith/XNL has rotated the spectra in the new wind direction with the energy focussed in the new young wind-sea. However, the old waves persist with small amounts of energy remaining in the westerly sector (unlike the observations).

The ST6/Smith/DIA on the other hand is slow to respond to the turning winds. For the 180° wind turn, the energy has split

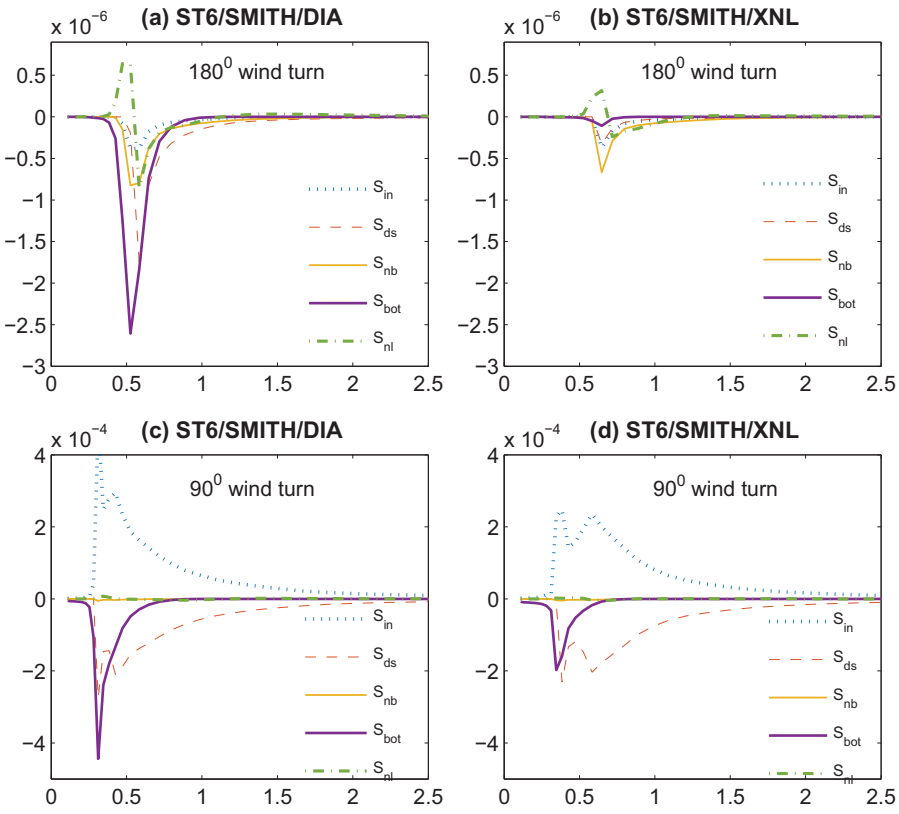

Fig. 9. One-dimensional spectral source terms for (a) ST6/Smith/DIA for the 180° wind turn; (b) ST6/Smith/XNL for the 180° wind turn; (c) ST6/Smith/DIA for the 90° wind turn; (d) ST6/Smith/XNL for the 90° wind turn.

approximately equally between the old and the young wave systems after about 20 min. Thereafter 30 min of wind shift, the measured and the modelled spectra have now further rotated from East to the North-east. While the decoupling of the old and the new wave system in the ST6/Smith/DIA is weaker, the process of the spectral rotation is similar to the measured spectra. The young sea develops under the wind input while the old sea decays under the influence of the dissipation terms.

The directional response of the Komen/JONSWAP DIA model lags behind the response time of the ST6/Smith/DIA by more than 15 min. It takes approximately 20 min after the 180° wind turn for the ST6/Smith/DIA to develop the young wind-sea while the Komen/JONSWAP takes more than 35 min. Whilst the Komen/JONSWAP DIA model has been known to perform well for conditions that it has been calibrated against, it is unable to perform as well in a finite-depth water environment where the wind is suddenly changing direction within minutes.

Both the modelled and measured spectra indicate that the high-frequency components align more quickly with the wind than the relatively low-frequency components for the 180° event. This is consistent with the numerical experiments of Young et al. (1987) and the analysis of wave directional measurements by Günther et al. (1981), van Vledder and Holthuijsen (1993), and Hasselmann et al. (1980). The ST6/Smith/XNL/DIA models shows a slightly different behaviour of the spectral peak from the observed spectra. For the models, a gradual shift of the spectral peak from higher to lower frequencies occurs after the wind has turned similar to that shown by the measured spectra.

The responses of the ST6/Smith/XNL, ST6/Smith/DIA, Komen/JONSWAP/DIA models and the observed wave spectra to the 90° wind shift are presented in Fig. 6b. Unlike the 180° turn, the angle between the wind and the waves is smaller, therefore, the old and the young waves are not fully decoupled in the directional space. With the gradual growth of energy in the new wind direction combined with the decay in the old wind direction, there is a smooth rotation of the mean wave spectrum toward the new wind direction. The differences in the spectral structure between the ST6/Smith/DIA and the ST6/Smith/XNL models are not as distinct as for the 180° case. Similarly there are smaller differences between the ST6/Smith/DIA and Komen/JONSWAP/DIA models for this case. However, it is noteworthy that while both the ST6/Smith/DIA/XNL spectra have rotated to the West-south-west sector (following the new wind direction) after 30 min of wind turning, the Komen/JONSWAP/DIA spectra has only managed to rotate to the West in this timeframe.

Young et al. (1987) observed similar rotation of spectra in response to wind shifts. Using idealized simulations, they report a bimodal spectra similar to the current study for wind shifts of 90° and greater. For wind shifts of less than 90°, they find that the non-directional spectrum is unimodal and attribute this to the strong non-linear interactions between old and young wave systems that are closer in directional space. The wave–wave interactions counteract the growth of the secondary peak and force the spectra toward the dominant unimodal waves which they say is “favoured” by the non-linear interactions.

4.2.3. *Evolution of one-dimensional spectra and source functions*

The evolution of the modelled spectral energy for the 180° wind turn is shown in Fig. 7. As seen in the two-dimensional spectra, the energy is first generated in the high frequency components in the new wave system. This is indicated by the formation of bimodal peaks in the one-dimensional spectra at times after the wind has turned by 180°. The secondary peaks in the Komen/JONSWAP/DIA

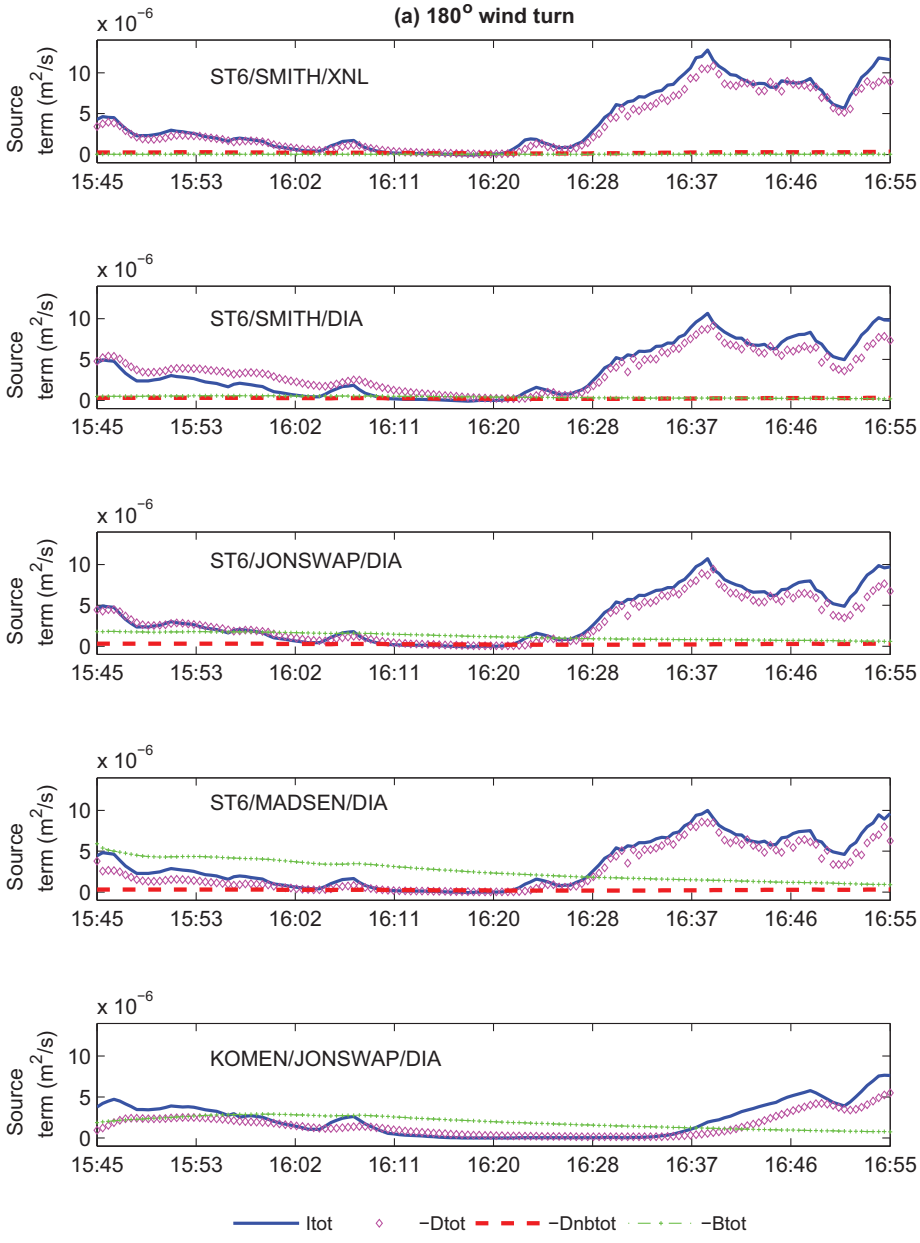

Fig. 10. Integrated source terms for (a) 180° wind turn; (b) 90° wind turn.

(Fig. 7c) model are weaker and occur at higher frequencies than the ST6/Smith/DIA (Fig. 7b). The bimodality of the spectrum is more pronounced in the ST6/Smith/DIA model than the ST6/Smith/XNL (Fig. 7a), which shows a weak secondary peak after 10 min and 15 min of wind shift. The secondary peak disappears after 20 min in the XNL model when the two peaks merge to form a unimodal distribution. Whilst the ST6/Smith/XNL performs well in transferring energy from the old to the new wave systems in the directional space, the model appears to be over-compensating the coupling of peaks in the frequency space when compared to the measured spectra. Fig. 8b (upper panel) shows that a distinct bimodal frequency distribution in the measured spectra exists 20 min after the 180° wind shift. The secondary peak continues to grow at the higher frequencies and the low-frequency peak gradually weakens. The 90° case (Fig. 8d) shows very weak bimodal peaks but no secondary peak in the measured or modelled spectra. Young et al. (1987) ascribe the lack of secondary peak in wind turns of less than 90° to strong nonlinear interactions as discussed in Section 4.2.2.

Fig. 9a,b shows the variation of the source terms with frequency during the 180° wind turn. A new feature of the ST6 is the swell dissipation term, S_{nb}. It becomes dominant when the spectral density (wave energy) falls below the critical threshold density beyond which S_{ds} becomes inactive. This occurs just prior to and during the turning of the wind by 180°, when the wind speed drops to less than 2 m/s. At this time the contribution from S_{in} is small, and S_{ds} is negligible. However, the waves continue to dissipate via the S_{nb}. The b_1 in the computation of S_{nb} is a free parameter and has been calibrated to a constant value of 0.0014 using altimeter data by Young et al. (2013). Zieger et al. (2015) have further tested the value of b_1 in a global hindcast using WAVEWATCH III® and found that there is considerable improvement in the model performance if b_1 is scaled against wave steepness from (11) instead of being assigned a constant value.

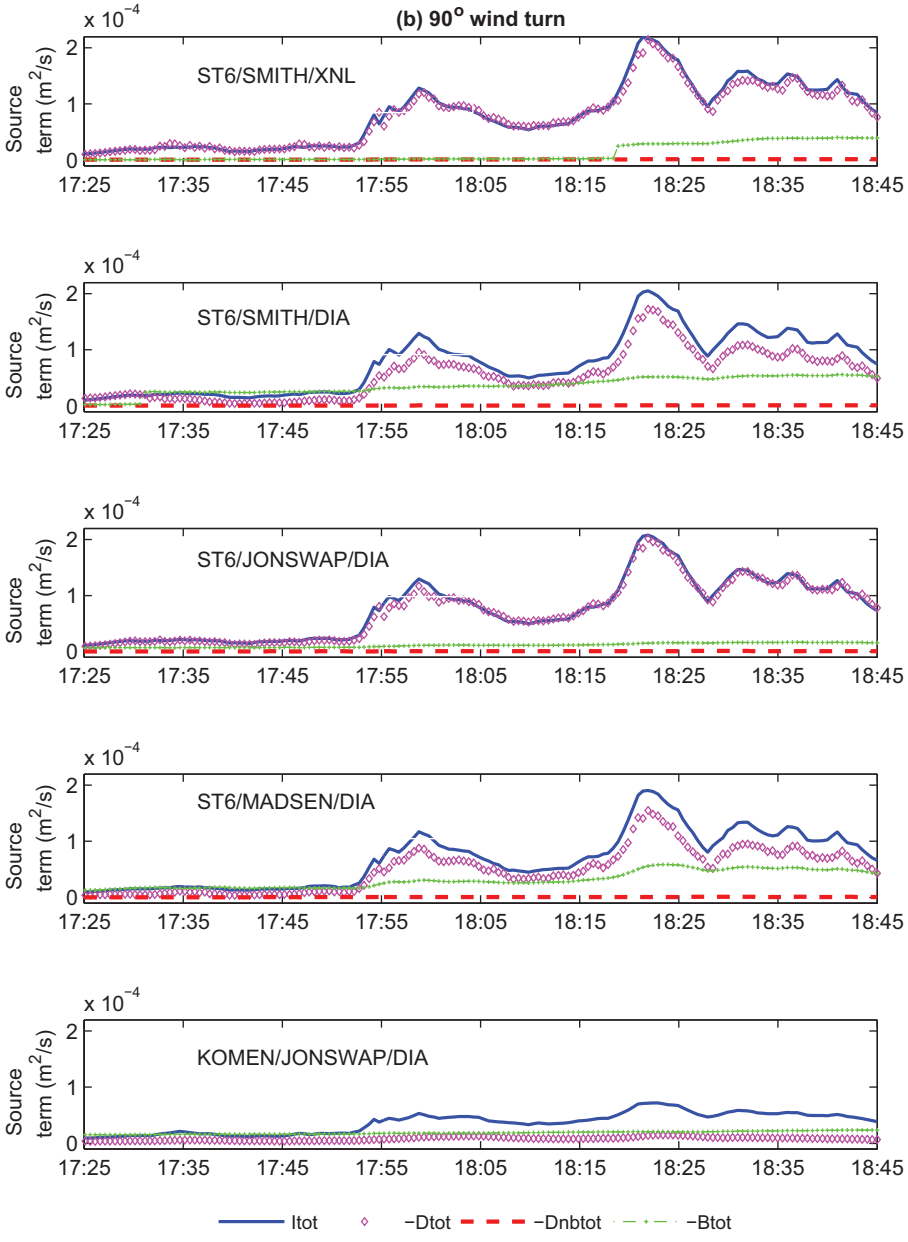

Fig. 10. Continued

Although the waves were present before the wind turn, the wind speeds were extremely low (below 2 m/s) immediately before and during the 180° wind turn, leading to low overall energy and low orbital velocities. This has an impact on the S_{bot} in the Smith model, where the ripple formation is dependent on the Shield's parameter and the criteria governing the threshold of sediment movement on the seabed described in Section 2.4. The Shield's parameter is a function of both the orbital velocity and grain size described in (14). At low wind speeds when the orbital speeds are low, the threshold of sediment movement is not exceeded, the sediment remains immobile and there is no ripple formation. Therefore, S_{bot} is significantly smaller relative to S_{bot} during strong winds. This differs from the friction models of JONSWAP and Madsen. The JONSWAP model is mainly dependent on a constant empirical factor (12), and the roughness length in the Madsen (13) model does not have a direct dependence on the site-specific sediment properties. In situations where the interaction with the bottom sediment is likely to influence the waves, the Smith model represents a more realistic physical process in comparison with the other friction models and this results in better accuracy.

For the 90° case (Fig. 9c,d), the formation of ripples and the subsequent sheet flow due to higher orbital speeds at wind speeds of 20 m/s and above after the wind turn results in an increased magnitude of S_{bot} in both the ST6/Smith/DIA and ST6/Smith/XNL models. In this case, S_{in} shows a bimodal frequency distribution but this is mirrored by the S_{ds} during and after the wind turn, therefore it does not result in a bimodal energy spectra. The S_{nb} is negligible for this case and the dissipation mainly occurs from S_{ds} with a significant contribution from S_{bot}.

Another new feature in the ST6 wind input term S_{in} is the negative input for cases of oblique and adverse winds. Zieger et al. (2015) describe two phases W_1 and W_2 (described in (3) and (4)) in an academic duration-limited wind turn case where the turn of the wind marks the beginning of the second phase. This feature is consistent with the negative input postulated by Tolman and Chalikov (1996) in the original WAVEWATCH source term.

During the wind shift of 180°, the existing waves oppose the wind and S_{in} shows a negative input (Fig. 8a,b). The W_1 from (3) for following winds is zero and therefore W from (2) is negative. The influence of negative input was evaluated by varying the negative input coefficient, a_o in (2) from 0.04 to 0.9 in the case of 180° wind turn when the impact of adverse winds is considered to be maximum. However, the increase in the negative component of the S_{in} (W_2 from (3)) is negligible when compared with other source terms and therefore, the overall influence of negative S_{in} is found to be insignificant for the two events.

The integrated source terms (over frequency and direction) for the 90° and 180° wind turns are presented in Fig. 10. The whitecapping dissipation, D_{tot} is the dominant mechanism for dissipation for both the 90° and 180° cases for the ST6/Smith models. The exception is during the 180° wind shift when the nonbreaking/swell dissipation D_{nbtot} and the bottom-friction dissipation B_{tot} have a greater influence than D_{tot} as discussed above.

The above is in contrast with the Komen/JONSWAP/DIA model particularly for the 90° case where the B_{tot} exceeds the D_{tot}. The D_{tot} in the ST6/Smith nearly always mirrors the I_{tot} in both magnitude and trend while for the Komen/JONSWAP DIA model, the magnitude of D_{tot} is very small, approximately 10% of the magnitude of I_{tot} for the 90° case. The I_{tot} for the Komen/JONSWAP DIA model is significantly weaker than the I_{tot} computed by ST6 models.

The ST6/JONSWAP/DIA, ST6/Madsen, and Komen/JONSWAP DIA models have a similar magnitude and trend for B_{tot}. The B_{tot} from these models provides significant contribution at all times while the B_{tot} in the ST6/Smith models shows more sensitivity to wind speed and the associated threshold of sediment movement via the orbital speed and the Shield's parameter. The ST6/Smith/XNL/DIA models compute a small B_{tot} when wind speeds are low during the 180° wind turn. The dissipation from B_{tot} for the Smith model increases during strong winds only. During low wind speeds, there is no sediment movement and the B_{tot} is only dependent on the sediment size. However, during strong wind conditions, the threshold of sediment movement is exceeded, leading to ripples formation or sheet flow, and thus resulting in larger dissipation from B_{tot}. This is evident in the 90° event (Fig. 10b) where the onset of the ripples and the sheet flow is shown by the jump in B_{tot} for the ST6/Smith/DIA/XNL models.

Although the B_{tot} shows a sudden jump in magnitude for both models, the jump occurs at different time. For the XNL, there is a sharp increase in B_{tot} approximately 15 min after the 90° wind turn while for the DIA, the increase in B_{tot} occurs before the wind turn. The variation in the timing of B_{tot} can be attributed to the three different stages of sediment mobility being encountered at different times in the DIA and XNL. The Smith model computes a different roughness factor for each of the three stages. The XNL model shows that the ripple formation only starts after the wind turn and gradually turns into sheet flow. On the other hand, the DIA model generates ripples much sooner than the XNL leading to a higher B_{tot} well before the wind turn. It is the effect of XNL on the spectral shape that forces the ripple formation to start later in the XNL model (van Vledder, 2015; personal communication).

5. Summary and conclusions

An extensive set of numerical simulations have been performed to determine the wave directional response to sudden changes in wind directions of 90° and 180°. The ST6 physics in combination with the Smith, JONSWAP, and Madsen friction models have been evaluated against the default Komen physics and the default bottom-friction (JONSWAP). Both the XNL and DIA solutions were used for the ST6/Smith model. The model results have been analysed at micro timescales of 30 s and micro spatial scales of less than 10 m. The high temporal and spatial resolutions enable a realistic prediction of the growth of young wind-sea spectra in Lake George which otherwise have a high probability of being missed in the averaging and smoothing processes over time-scales of 30 min or more and over larger spatial scales.

The model results have been compared against field data and standard non-dimensional wave growth rates for depth-limited cases. The ST6/Smith/XNL option shows the best performance in computing significant wave heights, peak periods, and directions. The ST6/DIA in combination with various friction models achieve a lower bias and RMSE than the Komen/JONSWAP/DIA model. The difference in RMSE between the ST6/Smith/DIA and Komen/JONSWAP/DIA models was computed as 0.01 and 0.04 for the 180° and 90° wind turns respectively. All tested models conform to the standard integral relationships between non-dimensional energy, non-dimensional frequency, and non-dimensional depth.

The directional response of the ST6 modelled spectra follows the observations of the spectra fairly well. The ST6/Smith/XNL and ST6/Smith/DIA models were found to have a response time of 10 min and 20 min respectively while the Komen/JONSWAP/DIA lagged behind with a response time of 35 min6 for the 180° wind turn. Both the measured and modelled two-dimensional spectra show that the high frequency components align faster with the new wind direction than the low frequency components. The spectra are bimodal for the 180° case but unimodal for the 90° wind turn. The young waves grow under the influence of wind input, S_{in} while the combined dissipation of S_{ds}, S_{nb}, and S_{bot} leads to the decay of the old waves. The ST6/Smith/XNL shows a faster alignment of young waves with the new direction and a stronger decoupling with the old wave system than the ST6/Smith/DIA.

The new terms for S_{ds}, and S_{nb} in ST6 combined with the S_{bot} from the Smith model results in a significantly different source term balance for the ST6/Smith models relative to the Komen/JONSWAP. The S_{bot} in the Madsen and JONSWAP models was found to be stronger and less dependent on wind speed than the S_{bot} in the Smith model. The aim of the paper was to test and validate the ST6 model, hence no attempt was made to change the default parameters of the Komen/JONSWAP/DIA model. It may be possible to tune the default Komen model to improve its performance. In contrast, the ST6 has very few tuning parameters. The ST6 parameterizations are tuned against measurements or against physical constraints. The wind input cannot be adjusted or tuned. The S_{ds} whitecapping dissipation has been calibrated by Rogers et al. (2012) where the a_1 and a_2 from (7) and (8) are based on physical considerations of the separation between inherent and cumulative dissipation. The S_{nb} non-breaking dissipation and the a_0 negative input allow some flexibility which can only be adjusted within the range of observed values for b_1 and a_0. In this respect, ST6 differs from the traditional wave models that have several tuning parameters.

The non-linear source term, S_{nl} was found to have a strong influence during the 180° wind turn where the magnitude of S_{nl} was predicted to be of the same order of magnitude as the other source terms. However, for the 90° wind turning event, the S_{nl} was predicted to be very small when compared with other source terms. Given the fact that the new wind has little interaction with the old waves, one would expect a larger role for the non-linear interactions. This does not happen in the case of the 90° wind turn event, and perhaps strong bottom dissipation is a reason here as discussed in the preceding section (Section 4.2.3). In deep water, the role of S_{nl} is likely to be more significant. Regardless of the technological advances and the frequent use of supercomputers, the XNL remains very computationally intensive, and therefore requires further investigation.

Although we expected the negative part of S_{in} to play a major role during wind turn events, it was observed to be comparable with the S_{ds} for only few minutes during the 180° wind turn event. The overall influence of negative S_{in} was found to be insignificant for the both 180° and 90° events. This will be considered in future studies.

The measured data were available from a single experimental site at Lake George, therefore we had to make an assumption regarding uniform wind fields across the lake. Nevertheless through sensitivity testing and using the observations to validate our model, we have been able to extract valuable indications on the performance of the different physical approaches that we have tested.

Acknowledgments

The funding for this study was provided by the Australian Research Council Discovery grant DP130100227 and the US Office of Naval Research grants N00014-13-1-0278 and N00014-13-WX-20825. The authors gratefully acknowledge the efforts of Dr. L. Cavaleri and Dr. G. van Vledder for their detailed reviews and recommendations that have led to a significant improvement of the manuscript. The contribution of the anonymous reviewer is appreciated. We thank Dr. S. Zieger of Swinburne University for the useful discussions and his comments on the manuscript. The Zieger swell dissipation formulation and negative wind input were implemented in the SWAN model by Dr. Y. Fan, post-doctoral fellow at Naval Research Laboratory. The simulations were performed on the gSTAR National facility at the Swinburne University of Technology. gSTAR is funded by the Swinburne University and the Australian Government's Education Investment Fund.

References

Ardhuin, F., Chapron, B., Collard, F., 2009. Observations of swell dissipation across oceans. Geophys. Res. Lett. 36 (L06607), 5.

Ardhuin, F., Roland, A., Dumas, F., Bennis, A.-C., Sentchev, A., Forget, P., Wolf, J., Girard, F., Osuna, P., Benoit, M., 2012. Numerical wave modelling in conditions with strong currents: dissipation, refraction and relative wind. J. Phys. Oceanogr. 12 (42), 2101–2120.

Babanin, A.V., Banner, M.L., Young, I.R., Banner, M.L., 2001. Breaking probabilities for dominant surface waves on water of finite constant depth. J. Geophys. Res. 106 (C6), 11659–11676.

Babanin, A.V., Young, I.R., 2005. Two-phase behaviour of the spectral dissipation of wind waves. In: Proceedings of the Ocean Waves Measurement and Analysis, Fifth International Symposium WAVE2005. Madrid, Spain CEDEX, Paper 51.

Babanin, A.V., Banner, M.L., Young, I.R., Donelan, M.A., 2007. Wave follower measurements of the wind input spectral function. Part 3. Parameterization of the wind input enhancement due to wave breaking. J. Phys. Oceanogr. 37, 2764–2775.

Babanin, A.V., Makin, V.K., 2008. Effects of wind trend and gustiness on the sea drag: Lake George study. J. Geophys. Res. 113 (C02015), 18.

Babanin, A.V., Tsagareli, K.N., Young, I.R, Walker, D.J., 2010. Numerical investigation of spectral evolution of wind waves. Part 2. Dissipation function and evolution tests. J. Phys. Oceanogr. 40 (4), 667–683.

Babanin, A.V., 2011. Breaking and Dissipation of Ocean Surface Waves. Cambridge University Press, p. 480.

Banner, M.L., Babanin, A.V., Young, I.R., 2000. Breaking probability for dominant waves on the sea surface. J. Phys. Oceanogr. 30, 3145–3160.

Bretschneider, C.L., 1958. Revised wave forecasting relationships. In: Proceedings of the 6th Conference on Coastal Engineering. Gainesville/Palm Beach/Miami Beach, FL, ASCE, New York, pp. 30–67.

Booij, N., Ris, R.C., Holthuijsen, L.H., 1999. A third-generation wave model for coastal regions. 1. Model description and validation. J. Geophys. Res. 104 (C4), 7649–7666.

Collard, F., Ardhuin, F., Chapron, B., 2009. Monitoring and analysis of ocean swell fields from space: new methods for routine observations. J. Geophys. Res. 114 (C07023), 15.

Donelan, M.A., Hamilton, J., Hui, W.H., 1985. Directional spectra of wind-generated ocean waves. Phil. Trans. R. Soc. Lond. A 315, 509–562.

Donelan, M.A., 1999. Wind-induced growth and attenuation of laboratory waves. In: Sajadi, S.G., Thomas, N.H., Hunt, J.C.R. (Eds.), Wind-Over-Wave Couplings: Perspectives and Prospects. Clarendon Press, pp. 183–194.

Donelan, M.A., Babanin, A.V., Young, I.R., Banner, M.L., McCormick, C., 2005. Wave-follower field measurements of the wind-input spectral function. Part I: Measurements and calibrations. J. Atmos. Ocean. Technol. 22, 1672–1689.

Donelan, M.A., Babanin, A.V., Young, I.R., Banner, M.L., 2006. Wave-follower field measurements of the wind-input spectral function. Part II: Parameterization of the wind input. J. Phys. Oceanogr. 36, 1672–1689.

Günther, H., Rosental, W., Dunckel, M., 1981. Directional wave spectra observed during JONSWAP 1973. J. Phys. Oceanogr. 11, 718–728.

Hasselmann, K., 1962. On the nonlinear transfer in a gravity wave spectrum, part 1. General theory. J. Fluid Mech. 12, 481–500.

Hasselmann, K., 1963. On the nonlinear transfer in a gravity wave spectrum, part 2. Conservation theory, wave-particle correspondence, irreversibility. J. Fluid Mech. 15, 273–281.

Hasselmann, K., Barnett, T.P., Bouws, E., Carlson, H., Cartwright, H., Cartwright, D.E., Enke, K., Ewing, J.A., Gienapp, H., Hasselmann, D.E., Kruseman, P., Meerburg, A., Müller, P., Olbers, D.J., Richter, K., Sell, W., Walden, H., 1973. Measurements of wind-wave growth and swell decay during the Joint North Sea Wave Project (JONSWAP). Dtsch. Hydrogr. Z. 12, A8.

Hasselmann, D.E., Dunckel, M., Ewing, J.A., 1980. Directional wave spectra observed during JONSWAP 1973. J. Phys. Oceanogr. 10, 1264–1280.

Hasselmann, S., Hasselmann, K., 1982. The wave model EXACT-NL. Ocean Wave Modelling. Plenum Press, New York, London The SWAMP Group, Chapter 24.

Hasselmann, S., Hasselmann, K., Allender, J.H., Barnett, T.P., 1985. Computations and parameterizations of the nonlinear energy transfer in a gravity-wave spectrum. Part II: Parameterizations of the nonlinear energy transfer for application in wave models. J. Phys. Oceanogr. 15, 1378–1391.

Jonsson, I.G., 1966. Wave boundary layers and friction factors. In: Proceedings of the 10th International Conference on Coastal Engineering, ASCE. Tokyo, Japan, pp. 127–148.

Komen, G.J., Hasselmann, S., Hasselmann, K., 1984. On the existence of a fully developed wind-sea spectrum. J. Phys. Oceanogr 14, 1271–1285.

Komen, G.J., Cavaleri, L., Donelan, M., Hasselmann, K., Janssen, P.A.E.M., 1994. Dynamics and Modelling of Ocean Waves. Cambridge University Press, p. 532.

Madsen, O.S., Poon, Y.K., Graber, H.C., 1988. Spectral wave attenuation by bottom-friction: theory. In: Proceedings of the 21st International Conference on Coastal Engineering, ASCE, pp. 492–504.

Manasseh, R., Babanin, A.V., Forbes, C., Rickards, K., Bobevski, I., Ooi, A., 2006. Passive acoustic determination of wave-breaking events and their severity across the spectrum. J. Atmos. Ocean. Technol. 23 (4), 599–618.

Nielsen, P., 1981. Dynamics and geometry of wave-generated ripples. J. Geophys. Res. 86 (C7), 6467–6472.

Nielsen, P., 1992. Coastal Bottom Boundary Layers and Sediment Transport, Advance Series on Ocean Engineering. World Scientific.

Phillips, O.M., 1984. On the response of short ocean wave components at a fixed wavenumber to ocean current variations. J. Phys. Oceanogr. 14, 1425–1433.

Quanduo, G., Komen, G., 1993. Directional response of ocean waves to changing wind direction. J. Phys. Oceanogr. 23 (7), 1561–1566.

Rogers, E.W., Babanin, A.V., Wang, D.W., 2012. Observation-consistent input and whitecapping dissipation in a model for wind-Generated surface waves: description and simple calculations. J. Atmos. Ocean. Technol. 29, 1329–1346.

Smith, G., Babanin, A.V., Riedel, P., Young, I.R., Oliver, S., Hubbert, G., 2011. Introduction of a new friction routine into the SWAN model that evaluates roughness due to bedform and sediment size changes. Coastal Eng. ASCE 58, 317–326.

SWAN Team, 2014. SWAN scientific and technical documentation. SWAN cycle III version 41.01, Delft University of Technology, 126 pp. http://www.swan.tudelft.nl.

Taylor, P.A., Lee, R.J., 1984. Simple guidelines for estimating wind speed variations due to small-scale topographic features. Climatol. Bull 18, 3–32.

Tolman, H.L. 2014 The WAVEWATCH Dev. Group, 2014: User manual and system documentation of WAVEWATCH III® Version 4.18. Tech. Note, MMAB Contribution No. 316. National Center for Environmental Prediction. College Park, MD. http://polar.ncep.noaa.gov/mmab/papers/tn276/MMAB_276.pdf.

Tolman, H.L., Chalikov, D., 1996. Source terms in a third-generation wind wave model. J. Phys. Oceanogr. 26, 2497–2518.

Tsagareli, K.N., Babanin, A.V., Walker, D.J., Young, I.R., 2010. Numerical investigation of spectral evolution of wind waves. Part I: Wind-input source function. J. Phys. Oceanogr. 40, 656–666.

Van Vledder, G.Ph., Holthuijsen, L.H., 1993. The directional response of ocean waves to turning winds. J. Phys. Oceanogr. 24 (2), 177–192.

Van Vledder, G.Ph., 2006. The WRT method for the computation of nonlinear four-wave interactions in discrete spectral wave models. Coastal Eng. 53, 223–242.

Vincent, C.L., Hughes, S.A., 1985. Wind wave growth in shallow water. ASCE J. Waterways Port Coastal Ocean Eng 111, 765–770.

Young, I.R., 1988. A shallow water spectral wave model. J. Geophys. Res. 93, 5113–5129.

Young, I.R., 1999. Wind Generated Ocean Waves. Elsevier Ocean Engineering Series. Elsevier Science, p. 288.

Young, I.R., Hasselmann, S., Hasselmann, K., 1987. Computations of the response of a wave spectrum to a sudden change in wind direction. J. Phys. Oceanogr. 17, 1317–1338.

Young, I.R., van Vledder, G.Ph., 1993. A review of the central role of nonlinear interactions in wind-wave evolution. Phil. Trans. R. Soc. Lond. A 342, 505–524.

Young, I.R., Verhagen, L.A., 1996. The growth of fetch limited waves in water of finite-depth: Part 1. Total energy and peak frequency. Coastal Eng. 29, 47–78.

Young, I.R., Banner, M.L., Donelan, M.A., Babanin, A.V., Melville, W.K., Veron, F., McCormick, C., 2005. An integrated system for the study of wind wave source terms in finite-depth water. J. Atmos. Ocean. Technol. 22 (7), 814–828.

Young, I.R., 2006. Directional spectra of hurricane wind-waves. J. Geophys. Res. 111 (C08020), 1–14.

Young, I.R., Babanin, A.V., 2006. Spectral distribution of energy dissipation of wind-generated waves due to dominant wave breaking. J. Phys. Oceanogr. 36, 376–394.

Young, I.R., Babanin, A.V., 2006. The form of the asymptotic depth-limited wind wave frequency spectrum. J. Geophys. Res. 111 (C06031), 1–15.

Young, I.R., Babanin, A.V., Zieger, S., 2013. The decay rate of ocean swell observed by altimeter. J. Phys. Oceanogr. 43, 2322–2333.

Zieger, S., Babanin, A.V., Rogers, W.E., Young, I.R., 2015. Observation-based source terms in the third-generation wave model WAVEWATCH. Ocean Modell. http://dx.doi.org/10.1016/j.ocemod.2015.07.014 .